Montanuniversität Leoben

A Study on the Behavior of Interstitial Elements in Nickel Super-alloys

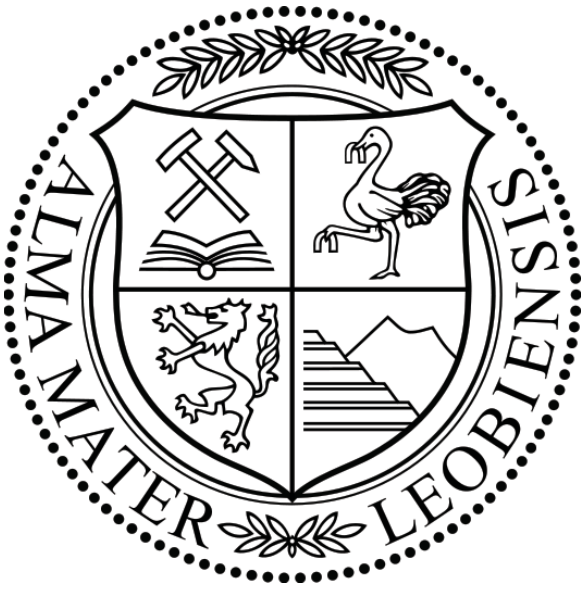

Diplomarbeit

von

Peter Wagner

Leoben, 17.05.2011 **Peter Wagner**

This Master Thesis was funded by Marschall Plan Scholarship Foundation of Vienna and the University of Leoben.

Affidavit

I declare in lieu of oath, that I wrote this thesis and performed the associated research myself, using only literature cited in this volume.

Eidesstattliche Erklärung

Ich erkläre an Eides Statt, dass die vorliegende Arbeit von mir selbständig und nur unter Verwendung der angeführten Literatur erstellt wurde.

Leoben, 17.05.2011 Peter Wagner

Acknowledgment

I would like to thank

Dr. mont. Peter Hosemann
Dr.mont. Gregor Mori
PhD. Stuart Maloy
PhD. Srinivasan Srivilliputhur
M.Sc. Darrin Byler

For the opportunity to develop my Master Thesis and helped me with words and deeds.

I also would like to thank all the people who helped me conducting my research in order to finish my thesis. For informative aid and helpful revision, I would like to thank Dipl.Ing. P. Scheibenbauer and Dipl.Ing. B.Yildrim of the RWTH Aachen.

Furthermore I would like to thank my family who supported me throughout all my years at the university and special regards to Anna Maria Scheibenbauer without whom I would have never been able to finish my Master Thesis.

A study on the Behavior of Interstitial Elements in Nickel Super-alloys

The overall aim of this work is to understand diffusion and distribution of interstitial and alloying additions in Ni_3Al through the combination of ab initio calculations and experiments. The results obtained from the Vienna Ab Initio Simulation Package (VASP) were compared with the data from high temperature carburization and high temperature oxidation experiments. The samples were characterized using optical microscopy, scanning electron microscopy, focused ion beam microscopy, energy dispersive X-ray spectroscopy, and other techniques. Despite limitations of system size of the VASP, it is able to efficiently predict the diffusion behavior of interstitial elements in well-ordered materials. For materials with a more random structure, the VASP results are not as exact, but using the received data as a basis could contribute to a far more accurate simulation behavior.

Eine Studie über das Verhalten von interstitielle Elementen in Nickelbasis Legierungen

Das Ziel dieser Arbeit ist es bessere Kenntnis über die Diffusion und die Verteilung von interstitiellen - und Legierungselementen in Ni_3Al mit Hilfe von Ab Initio Simulation und Experimenten zu erhalten. Die mittels Vienna Ab Initio Package (VASP) erhaltenen Resultate wurden mit Hochtemperaturkorrosionsversuchen (insbesondere Karburierung und Oxidation) verglichen. Die Proben wurden mittels Lichtmikroskopie, Rasterelektronen-mikroskopie, Feldionenmikroskopie und Röntgenphotoelektronenspektroskopie sowie anderen Charakterisierungsmethoden untersucht. Obwohl die Ab Initio Simulationen aufgrund der maximal verwendbaren Systemgrösse limitiert sind, war es doch möglich für geordnete Strukturen mittels der erhaltenen Daten ein Verhaltensmuster für interstitielle Elemente zu ermitteln. Diese Verhaltensmuster wurden durch die Experimente bestätigt. Für ungeordnete Systeme waren die ermittelten Daten nicht aussagekräftig, jedoch können diese als Ausgangswerte für zukünftige Berechnungen herangezogen werden.

Table of Contents

Table of Figures

Table Index

Introduction

Gas turbines used in jet engines and gas fired land – based turbines are an important accomplishment for current technology applications. While stationary gas turbines are used to produce electricity (a single unit can produce up to 480 MW [1]) gas turbines used in jet engines satisfy our need for fast and reliable transportation. In 2010, 751 million people were transported using gas turbine propelled planes [2].

Gas turbines are the most advanced energy conversion devices used. A cross section and the function of a gas turbine are shown in figure 1 [3]. It is usual to divide the gas turbine in two main parts, a cold and a hot section. In the cold section air is compressed and lead to the combustion chamber (hot section), where fuel is added and burned. The expanding hot gases are then used to operate the compressor stages in the cold section and as propellant.

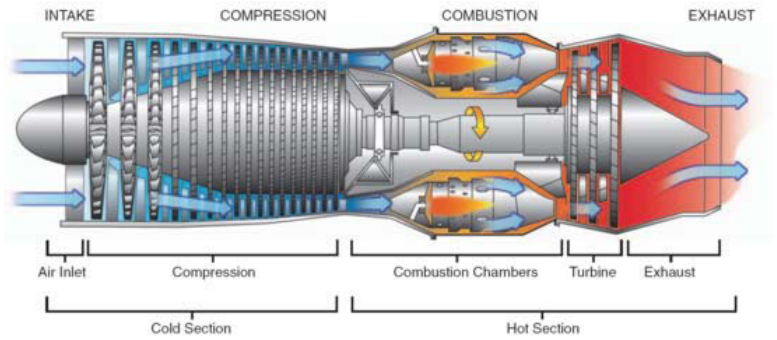

Figure 1 Cross section of a gas – turbine used in a jet engine [3]

A typical inlet temperature in a gas turbine engine exceeds 1450 K [1]. Furthermore, the thermodynamic efficiency of an engine is directly related to its operation temperature. Coping with such large temperatures is challenging for the materials used in turbine blades. In addition to high strengths, turbine blade materials must exhibit good creep and oxidation resistance. To increase the oxidation and heat resistance of the materials, the design of the turbine blades are optimized for confection-, film and effusion cooling. In order to maximise operating temperatures, the turbine blades can be coated with metal matrix composite or an intermetallic matrix composite or a ceramic matrix composite such as ZrO_2-6-8%Y_2O_3, a heat resistant oxide layer deposited on a “Bond Coat” (MCrAlY, PtAl) [4]. Figure 2 is a cross section of the turbine blade, displaying common structure and temperature gradients of a turbine blade [4].

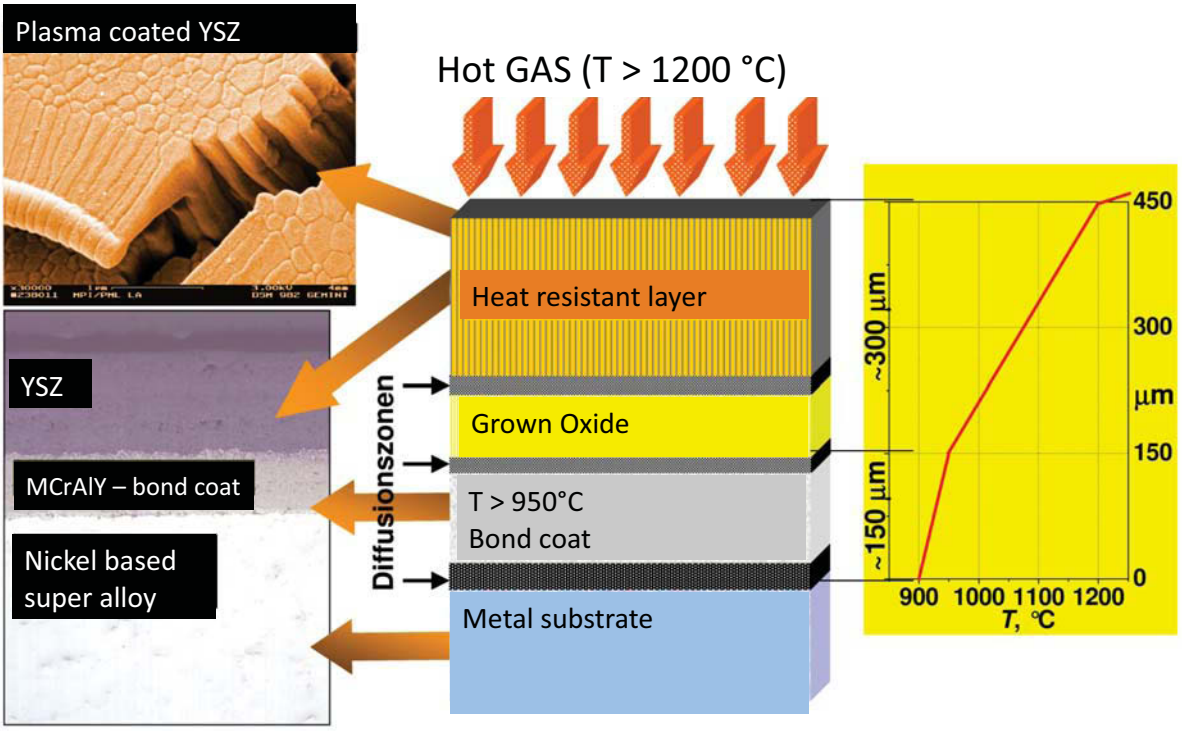

Figure 2 Structure usually used in a turbine blade [4].

Due to foreign object impact (FOI) - sand, bird - strike etc. - coatings might fail. Figure 3 [5,6,7] displays damaged blades due to FOI and residue, originating from common application of military transport plane.

In regards to jet engines, Nickel based super alloys are of preferred usage. The essential solutes in nickel based super alloys are aluminium and/or titanium. This generates a two-phase equilibrium microstructure consisting of random distribution of Al in Ni (NiAl gamma, γ) and ordered Ni_3Al (gamma-prime, γ') shown in figure 4.

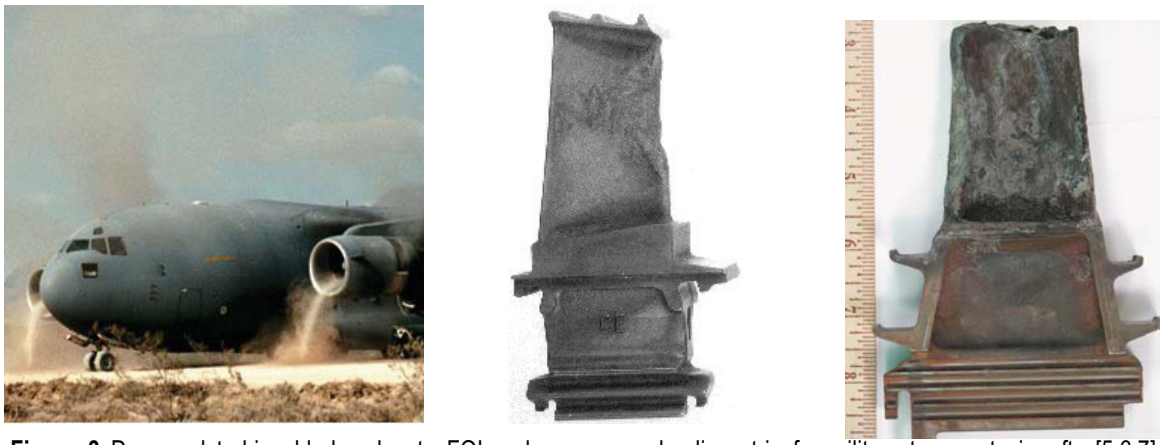

Figure 3 Damaged turbine blades due to FOI and a common landing strip for military transport aircrafts [5,6,7], indicating possible damage from environment.

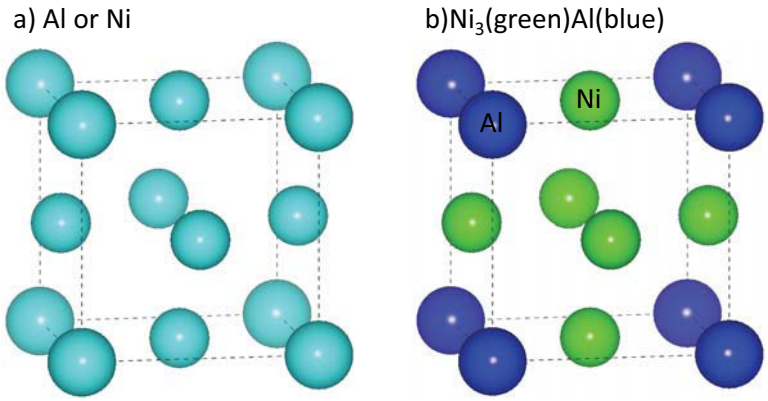

Figure 4 (a) face-centered-cubic (FCC) crystal structure of γ. (b) FCC crystal structure of γ'.

The γ' precipitate phase is largely responsible for the elevated-temperature strength of the material and its incredible resistance to creep deformation. The amount of γ' depends on chemical composition and temperature (fig. 5).

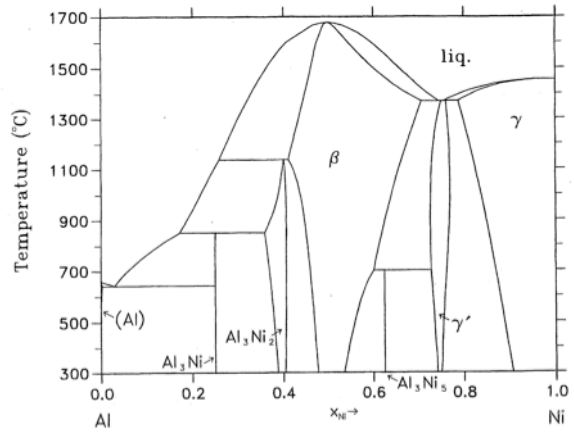

Figure 5 Calculated Ni-Al Phase Diagram [8]

The Ni-Al binary phase diagram shows the γ and γ' phase field. For a given chemical composition, the fraction of γ' decreases as the temperature is elevated. This behavior aids to dissolve γ' at a sufficiently high temperature (a solution treatment), followed by ageing at a lower temperature to generate a uniform and fine dispersion of these strengthening precipitates. However, as can be seen from the (γ+ γ')/γ' phase boundary on the isothermal ternary sections of the Ni-Al phase diagram, the γ' phase is not strictly stoichiometric. An excess of vacancies on one of the sub lattices may lead to deviations from stoichiometry. Alternatively, some of the nickel atoms might occupy the Al sites and vice-versa.

The small misfit between the γ and γ' lattices is important for two reasons. Firstly, when combined with the cube-cube orientation relationship, it ensures a low γ/γ' interfacial energy. The ordinary mechanism of precipitate coarsening is driven entirely by the minimization of total interfacial free energy. A coherent or semi-coherent interface therefore makes the microstructure more stable at elevated temperatures. The misfit can be controlled by altering the chemical composition, particularly the aluminum or titanium ratio. A negative misfit stimulates the formation of γ' rafts (essentially layers of the phase in a direction perpendicular to the applied stress). This can help reduce the creep rate if the mechanism involves the movement of dislocations across the precipitate rafts (fig. 6) [7].

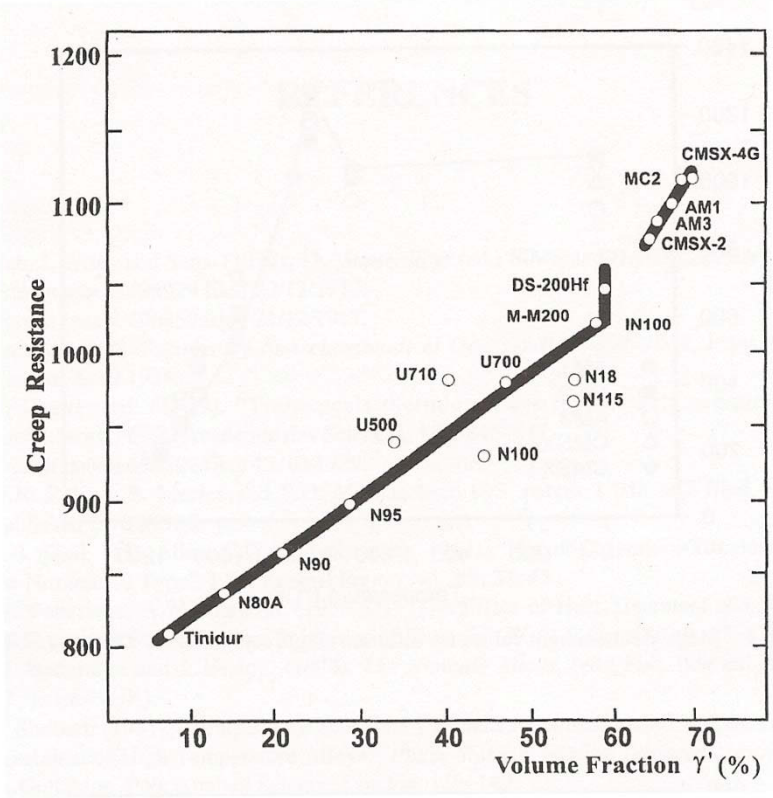

Figure 6 Evolution of creep resistance of all types of super alloys with Ni_3Al volume fraction (100 hours creep rupture strengths under 125 MPa) [8].

This thesis is aimed to predict the behavior of interstitial elements (C, Cl, N, O), which do occur during normal operation conditions, while burning gas. The elements are introduced into the Ni based super alloy once the corrosion or thermo coating is damaged. Areas, which are most likely to suffer from the influence of the interstitial elements and which are therefore most likely the origin of failure, are going to be identified using ab initio calculations. In order to attain an improved understanding of the results obtained by ab initio calculations, the Vienna ab initio theory conjointly with the steps necessary to conduct the calculations is going to be presented.

The simulated results are compared to experimentally obtained data of high temperature corrosion tests (carbon and oxygen).

The overall aim is to create a starting point for future studies concerning the influence of interstitial elements using ab inito calculations. Being able to predict possible threats to the material could help to design an alloy suitable for the task or at least help to reduce number of possible materials and therefore decrease experimental effort.

1. Theory

1.1 Theory of Vienna Ab Initio Simulation

The Vienna ab initio simulation program centers on a theory invented by Kohn, allowing for the successful prediction of the total energy of a system *E* in [eV] (such as a solid or a molecule). The energy is solely dependant on its systems electron density of its ground state, which occurs at 0 Kelvin. To achieve a more realistic simulation, effects such as spin polarization and impact of relativism have to be taken into account.

The development of this theory made it possible to understand and simulate electronic, structural and dynamic properties of matter. Thus, the atomic nuclei are defining the electron density and the total energy *E*:

$$E = E\left[\rho(r),\{R_\alpha\}\right] \tag{1}$$

The set R_α denotes the positions of all atoms α in the systems. ρ signifies the electron density, which acts as a scalar function; defined at each point r in real space for solid-state systems $\rho(r)$:

$$\rho(r) = \sum_i n_i \left|\Psi_i(r)\right|^2 \tag{2}$$

n_i is the occupation number of electrons of the Eigenstate i, which is represented by the one-particle wave function Ψ_i [8, 9].

The Density Functional Theory (DFT), used in VASP, is based on the assumption that the motions of the electrons are infinitely faster than those of the nuclei. This assumption does not simplify the already quite complex problem of simulating a structure, considering the fact that the i^{th} electron depends, in a nonlinear way, on the single wave functions of all the other electrons.
Hohenberg and Kohn advanced the concept that the total energy of a many - body system might be divided in three parts: a kinetic energy T_0, electrostatic or Coulomb energy *U*, and the so-called exchange correlation energy E_{XC}:

$$E = T_0 + U + E_{XC} \tag{3}$$

The Coulomb energy *U* contains the electrostatic energy, describing the interaction between electrons and nuclei, the repulsion between all electronic charges and the repulsion between nuclei. The kinetic energy term T_0 is the sum of the kinetic energies of all "effective" electrons. Effective electrons simulate the charge, mass and density distribution of "real" electrons of a system, while further acting as independent particles, while real electrons substantially depend - in a non linear way - on the single wavefunctions Ψ of all other electrons:

$$T_0 = T[\rho(r)] \tag{4}$$

The term E_{XC} is the so-called "exchange-correlation energy", and includes all remaining electronic contributions to the total energy. The key assumption of the exchange correlation energy is that the electrons in the solid do behave like electrons in a gas with exact same density, which is defined using the gas exchange – correlation function $\in_{XC}$. The Pauli principle is applied on on electrons and defines that each electron inhabits a specific line-up of the four quantum numbers s, p, d and f-states, which causes them to exhibit opposing spins; thus all electrons, which share the same spin, avoid each other. Therefore, the average Coulomb repulsion, inflicted on the electron, is reduced. This additional multiple component interaction term between electrons of opposite spin, is smaller than the exchange energy, but has as a major impact on the determination of length and strength of interatomic bonds. This effect can be noticed in regards to electrons, located near an atomic nucleus. Those electrons achieve such high kinetic energies that relativistic effects become noticeable. While it is possible to neglect the relativistic effect for light elements, it is necessary to include these effects above the atomic number of 54 [8,9]. E_{XC} can therefore be written as follows:

$$E_{XC} = E_{XC}[\rho(r)] = \int \in_{XC} (\rho(r)) d^3r \tag{5}$$

The energy minimizing density *ρ(r)* is retrieved via the usage of the derivative of the total energy *E* of a system:

$$\frac{\partial E}{\partial \rho(r)} = 0 \tag{6}$$

This leads to a single-particle equation, called the Kohn-Sham equation [8, 9]:

$$\left[-\frac{\hbar}{2m}\nabla^2 + V_{eff}(r)\right]\Psi_{i(r)} = \in_i \psi(r) \tag{7}$$

$\in_i$ denotes the Eigenvalue, $\psi(r)$ is the one particle function, ħ = h/(2π) and h is the Planck constant. $V_{eff}(r)$ is the effective potential, consisting of the Coulomb or electrostatic potential $V_C(r)$ at point r and is generated from the electric charges off all nuclei and electrons in the system, and the exchange-correlation energy E_{XC}:

$$V_{eff}(r) = V_C(r) + \int \frac{\rho(r')dr'}{|r - r'|} + \frac{\partial E_{XC}}{\partial \rho(r)} \tag{8}$$

This advancement turns the original many - body problem into a series of effective single-particle Schrödinger equations [8, 9].

Eigen values due not play an important roll in the density functional theory, however the one-electron theorem offers great advantages henceforth it's almost irresistible not to exploit the Kohn-Sham theorem as far as possible.
In the Kohn-Sham equations, each wave function has an associated eigenvalue $\in_i$ with an occupation number of n_i. Janak's theorem [8, 9, 10] establishes a relationship between the total energy and these eigenvalues.

$$\in_i = \frac{\partial E}{\partial n_i} \tag{9}$$

The eigenvalue $\in_i$ equals the change of the total energy with the change of the occupation number of level i.

The possibilities of how to use the derivate of the single-particle equation are almost limitless; receiving the force acting on an atom, which identifies the most stable structure or enables to study dynamical processes such as diffusion etc.

1.1.1 Position File

To create a position file, the so-called POSCAR, for VASP, several problems have to be considered:

(i) Matrix of the system
(ii) how many elements in the system
(iii) substitution or interstitial elements
(iv) strongly ordered or random ordered alloy
(v) positions of the elements
(vi) lattice parameters

How those factors influence the position file is best examplified in 4x4x4 nickel super-cell (Fig. 7). The dimensions of a unit cell are 3.523 x 3.523 x 3.523 [Å] and consists of 4 Ni atoms. The creation of 4x4x4 nickel super-cell requires 4x4x4 unit cells next to each other, thus receiving a cuboid with a length of the edge of 14.093 [Å]. This cuboid consists of 256 Ni atoms in a simple P1 configuration and a lattice parameter of the unit cell of 3.523 [Å].

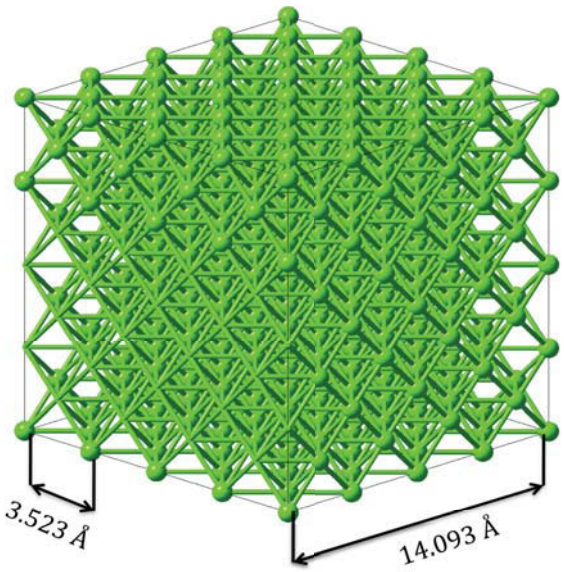

Figure 7 4x4x4 super cell with a lattice parameter of 3.523 [Å] and an overall length of 14.093 [Å]

To implement any impurity in this system, the lattice site of the impurity in Cartesian coordinates must be calculated. Those coordinates are subsequently transformed in absolute coordinates, which then can be used by VASP. By implementing a point defect into the matrix the resulting energy is called “point defect formation energy”.

1.1.2 Input File

The input file or INCAR provides the VASP with the parameters necessary for starting and running needed calculations.

The parameters of the INCAR file are provided for an individual task, which will be used by the program. It defines the step size, accuracy and other parameters, required to conduct calculations. The compatibility between the files is of outermost importance. The importance of this file might be better explained using an example.

DFT simulations were, for some time, restricted to non-spin-polarized cases. This limitation however, did affect many systems and compounds such as magnetic transition in metals. A spin-polarized method was therefore required, which enabled the use of electrons with “spin-up” and “spin-down” configuration. This problem was solved using the Local Spin Density (LSD) approximation [8,11,12,13]. The spin density $\sigma(\boldsymbol{r})$ is defined as the difference between the density of spin-up electrons and the density of spin-down electrons; $\rho(\boldsymbol{r})$ denotes to the electron density while:

$$\sigma(r) = \rho_{\uparrow}(r) - \rho_{\downarrow}(r) \tag{10}$$

Because the effective potential used for the simulation depends on the spin and spin up - spin down; thus the local spin density function theory exhibits a tremendous influence. In case of spin - up and spin – down, densities turn zero throughout space; the local spin density function becomes identical with the local density function [8].

Usage of the local spin density function is defined in the input file. The commands and possibilities for the input file, used in VASP, can be researched on the VASP research homepage and are updated on a regular basis. VASP user groups are interactive, evolving the simulation program constantly, henceforth it might be necessary to conduct regular online research to perform new simulation approaches such as the nudge elastic band simulation. The key commands of this simulation are also defined in the input file, but as seen before, those few new command lines open up a new possibility to simulate dynamic events such as diffusion in an atomistic scale.

1.1.3 K - Point Grid

The Brillouin zone is of main importance for VASP calculations. Each Brillouin zone is different for various crystal structures (fig. 8), as it is a uniquely defined primitive unit-cell of the crystal structure in reciprocal space. The first Brillouin zone is usually used for simulation calculations, nevertheless there are a second and a third Brillouin zones, corresponding to a sequence of separated regions at increasing distances from the origin. Those zones are rarely used due to symmetry. Hence, the first Brillouin zone is often referred to as “the Brillouin zone”. The Brillouin zone further defines a certain area with a distinct range of electron bands. Those band structures define several characteristics (electronic and optical characteristics etc.) of the material. They have different widths based on the atomic orbital or maybe allowed to overlap in order to create a new larger single band (fig. 9).

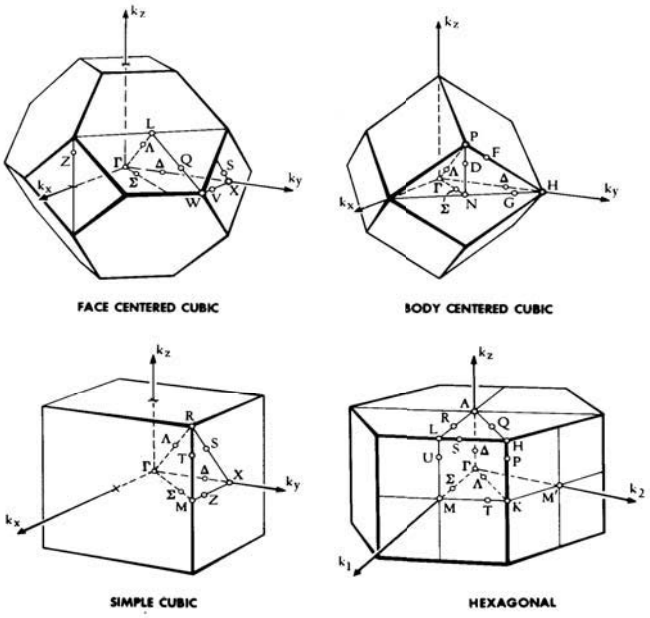

Figure 8 Brillouin Zone for different crystal structures. [14]

The K-Point file creates a k-mesh inside the first Brillouin zone to locate the parameters of the electron bands. The more accurate or finer the k-mesh (also known as k-grid), the more accurate the obtained results will be. Until a certain point of accuracy is reached, all further attempts, using an even finer k-mesh, do not result in overly precise results, but in an increase of time, which is necessary to calculate the system. The increased accuracy in terms of results is therefore not relevant.

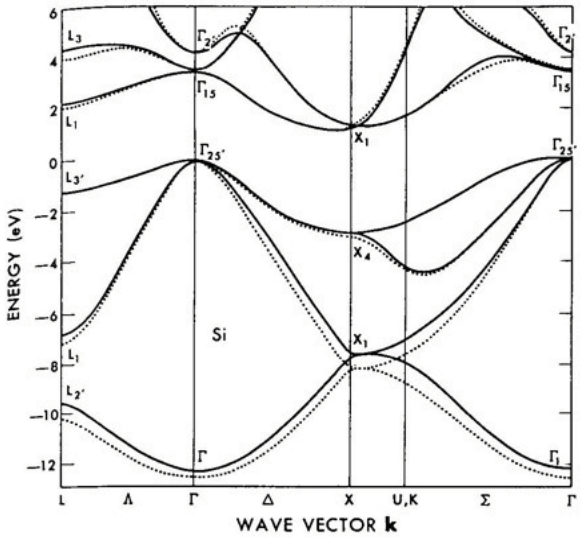

Figure 9 Illustration of electron bands and Brillouin zones in a material, in this case Si. [15]

1.1.4 Pseudo Potential File

The POTCAR file contains the pseudo-potential (alternatively called the “effective potential file”) for each atomic species, which is used in the simulation of the system. It is an attempt to replace the complicated impact of the core electron motion and its nucleus with a simplified version (effective/pseudo potential), which is then used in the Schrödinger equation instead of the far more complex Coulomb potential (Fig. 10).

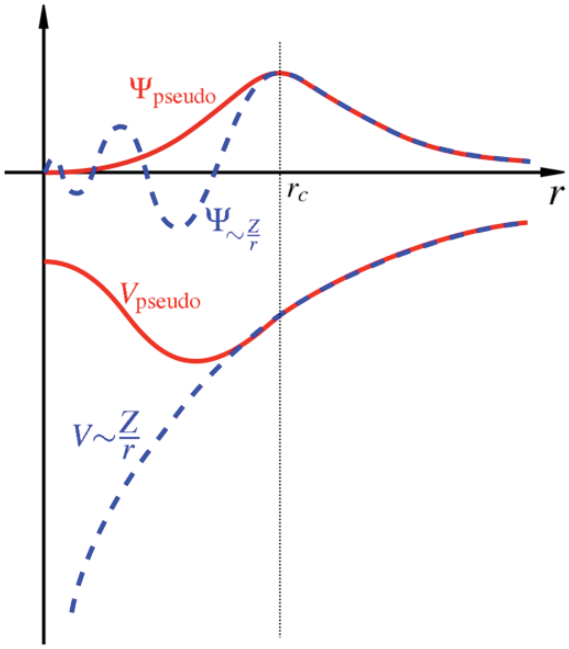

Figure 10 Comparison of a wave function and Coulomb potential of the nucleus (blue) to a pseudo wave function and Coulomb potential (red). The real and the pseudo wave function / potentials match above a certain cut-off radius r_c [16]

The pseudo-potential files used in VASP deal only with the active valence electrons, while the core electrons are considered to be a nucleus and are therefore excluded from the equation [8, 9, 16]. To perform atomic scale simulation, the local density approach or LDA for the creation of pseudo-potential files is often employed, which allows for the assumption that the exchange and correlation effects do not strongly depend on the variations of the electron density in the vicinity of *r*. It is proven that an approach via LDA provides results of interatomic bond lengths for various solids, surfaces and molecules. However it can be observed, that most lattice parameters and weak bonds are too short and that the binding energies calculated, are typically too large. Howbeit, gradient-corrected density functions or GGA offer a remedy. The basic idea of these potentials is the inclusion of terms in the exchange-correlation expression, which depends on the gradient of the electron density and not only on its value at each point in space. Therefore, these corrections are also referred to as “non-local” potentials [8,17,18].

1.2 High Temperature Corrosion

High temperature corrosion is defined as the deterioration of a material, especially of metals and alloys, due to the exposure to gases or liquids at high temperatures. Knowledge of behavior of materials in high temperature environments is of outermost importance to avoid material failure. This chapter provides a short overview on high temperature corrosion, which is most common for nickel based super alloys.

1.2.1 Oxidation of Metals

The first step in the oxidation of metals is the adsorption of oxygen. The oxygen atom is bonded to the metal surface using a free linkage between the atoms. This linkage is usually very strong and can be compared to a chemical bond. The adsorption of oxygen towards metal is slightly more negative than the enthalpy of oxygen, therefore preferable for the system.

During numerous studies, it was shown that nucleation needs a specific incubation time before an oxide layer starts to grow on the surface and starts affecting the material. The steps necessary are shown below [19]:

(i) An incubation time for a nucleus is set. Until this time is reached, the surface is unaffected.
(ii) Lateral nuclei growth starts only, when the whole surface is covered with an oxide layer.
(iii) The oxide layer starts growing vertically over the whole sample.

The incubation time depends on several factors: temperature, partial pressure of oxygen and nucleation orientation (epitaxic growth). The number of nuclei is increasing, depending on an increasing oxygen partial pressure and rising temperature. Therefore a higher partial pressure results in a denser oxide layer and more nuclei thus.

The number of nuclei and the growth of the oxide layer is further dependent on the epitaxy. Epitaxic growth is known to form a very dense layer parallel to the surface of the substrate, with a parallel order of high atomic and ionic density. For an epitaxic growth, it is necessary that the lattice parameters between the substrate and the oxide layer only have a small mismatch. If the mismatch of the lattice parameters is too big, the internal stress of the layer

is going to be reduced by plastic deformation and by introducing defects in the oxide layer such as voids and cracks.

Materials used in high temperature application are supposed to have parabolic oxide layer growth (aluminum, nickel, chromium). The parabolic oxidation law can be defined as follows

$$\left(\frac{\Delta m}{A}\right)^2 = k_p * t \tag{11}$$

Δm equals the gain of mass, A is the whole sample area and k_p is the parabolic oxidation constant defined by mass increase [$kg^2m^{-4}s^{-1}$] [20,21]. It can be considerably transformed, depending on the thickness of the oxide layer:

$$s^2 = k_p' * t \tag{12}$$

s is the thickness of the layer, k_p' is the parabolic oxidation constant depending on the thickness of the oxide layer defined by the oxide layer thickness over time [m^2/s] [20,21]. The parabolic oxidation constant k_p and the scale thickness, depending parabolic growth constant k_p', can be linked as followed [21]:

$$k_p = k_p'\left(\frac{m_{Ox}}{\rho_{Ox} * \Delta m}\right)^2 \tag{13}$$

m_{Ox} and ρ_{Ox} denote the mass and the density of the oxide and Δm to the change in mass. Common knowledge suggests that the scale growth is diffusion-based, dependent on temperature T. It is thus possible - using a pre-factor k_{p0} - to formulate [21]:

$$k_p = k_{p0} * e^{-\frac{Q}{RT}} \tag{14}$$

Q denotes the activation energy necessary for diffusion and R the gas constant.

Relating to the theory of C. Wagner, the scaling resistance is increased by a low diffusion coefficient, which is the case for Cr_2O_3 and Al_2O_3. Therefore chromium and aluminum are recommended as alloying elements for high temperature materials.

In nickel-based, chromium-aluminum-rich super alloys, the oxidation behavior is quite complex. To ease into the topic of selective corrosion, the corrosion of nickel – chromium alloys is observed, continued with the more complex topic of a nickel - chromium - aluminum alloy.

Nickel chromium alloys, with low chromium contents, tend to exhibit internal corrosion forming Cr_2O_3 islands within the bulk material, while an outer layer of NiO is formed. Within the inner NiO layer, which happens to be porous sometimes, $NiCr_2O_3$ precipitates can be allocated (fig. 11). This layer contains Cr ions; in solution and in equilibrium the $NiCr_2O_3$ precipitates. This behavior, also called “doping effect”, provides cation vacancies, hence increasing the mobility of Ni atoms [22,23]. V_{Ni}^{2-} are nickel vacancies with a negative charge of minus 2, while h stands for a hole, in this case with a positive charge.

$$\frac{1}{2}O_2 = O_O + V_{Ni}^{2-} + 2h^+ \qquad (15)$$

If the chromium content of the material is increased to about 10 wt%, the oxidation behavior is altered and the oxidation rate falls towards values more typical for chromium than of nickel. With chromium contents higher than 15 wt%, a chromium oxide layer is formed. The chromium layer is formed, depleting the chromium concentration inside the bulk material. If the layer is damaged, a chromium-depleted material is exposed, which leads to internal oxidation and formations of NiO. Because of the depletion effect, oxidation resistant alloys, based on Ni-Cr, usually use up to 18 – 20 wt% Cr [22,23].

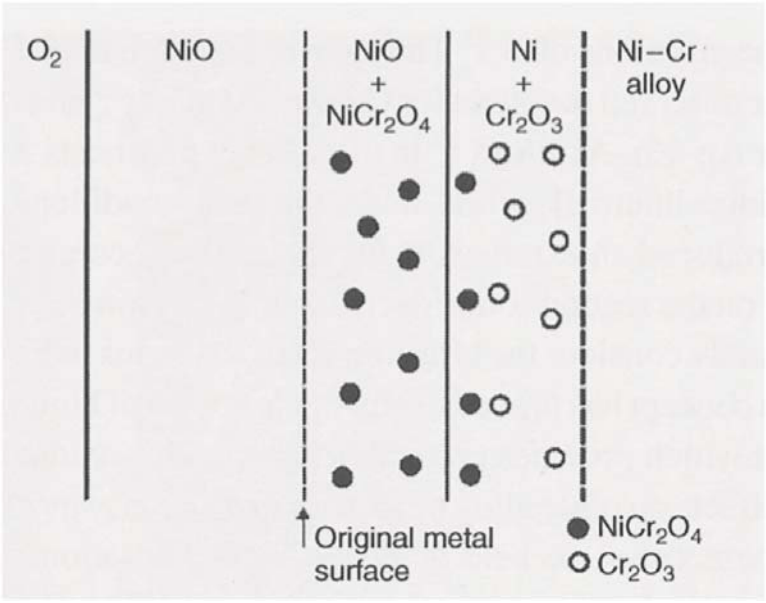

Figure 11 Schematic diagram of the oxidation morphology of diluted Ni-Cr alloys [22].

The behavior of chromium explained earlier might be called a steady - state oxidation. In this case it suggests that even if a chromium concentration above the critical value is exposed to an oxidizing atmosphere, nickel oxides as well as chromium oxides are going to be formed in the initial stages. Because NiO and $NiCr_2O_3$ grow much faster than a Cr_2O_3, a significant amount of those oxides can be formed until a continuous Cr_2O_3 layer can be formed. This stage of oxidation is also called transient oxidation [22,23] and occurs for almost all systems, which contain oxides, which receive a lower more stable free formation energy forming oxides. Figure 12 displays a schematic drawing of such a case, where both elements A and B form stable oxide layers, but the oxide AO is less stable than the BO oxide. Case (a) displays a case in which the concentration of B is too low to form a continuous oxide layer and is therefore a case of internal oxidation such as a Ni-Cr alloy with less than 10 wt% of chromium. In a simple case, if B forms a very stable oxide and $D_B \ll D_O$ the depth of the internal oxidation can be calculated as followed:

$$X(t) = \left(\frac{2N_O^{(s)} D_O t}{N_B^{(0)}} \right)^{\frac{1}{2}} \tag{16}$$

D_B is the diffusion coefficient for material B and D_O is the diffusion coefficient for oxygen. $N_B^{(s)}$ denotes for the concentration of B in the bulk material. X defines the depth of internal oxidation in correspondence to time t.

It is obvious that the depth of the possible internal oxidation depends on $N_B^{(s)}$, hence it is possible to assume that a continuous BO surface layer can be formed if $N_B^{(s)}$ surpasses a critical value $N_B^{(s)} \gg N_B^{(critical)}$, which would precede to case (b) [24]. In case (b), the concentration of B is high enough to form a continuous layer, but due to the transit state it was possible that a few OA oxides were able to form.

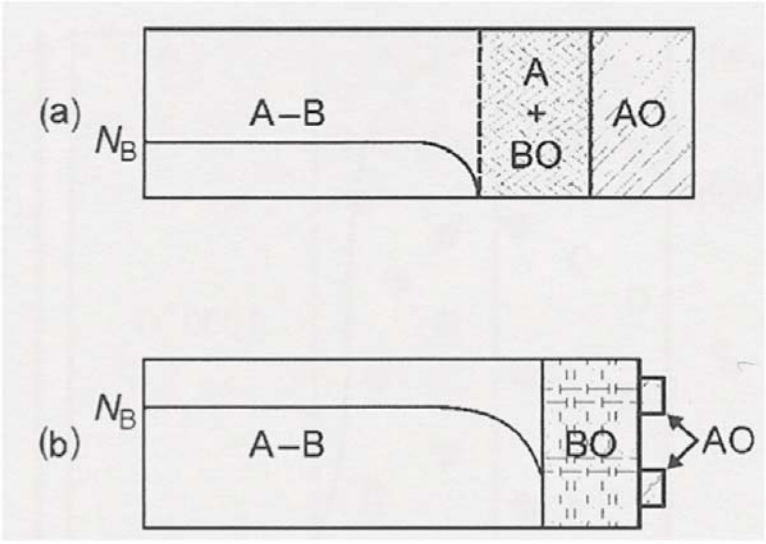

Figure 12 Schematic diagram of the oxidation of an alloy AB for which both elements form stable oxides. In (a) oxide A is formed, but concentration of element B is too low, which leads to an internal oxidation while in case (b) a continuous B oxide scale is formed. [21].

Newer developments in materials using in high temperature applications are known to be Ni-Cr-Al based super alloys. The oxidation behavior differs from the oxidation behavior explained earlier, but the same model can be used in order to describe the mechanism of the oxidation layer growth. Ni-Cr-Al alloys can be divided into 3 basic groups. Group 1 contains mainly Ni and therefore fewer Cr and Al, while group 2 consists a higher concentration of chromium and group 3, which possess an equally balanced chromium and aluminum concentration.

In group one, nickel dominated growth forms a continues NiO layer on the surface of the material followed by internal oxidation of Al and Cr and or a $Ni(Al,Cr)_2O_4$ sub - layer. At the beginning of the oxidation, during the transit state, all materials develop an oxide scale, yet NiO dominates the growth outwards while deeper inside the bulk of the material, Cr_2O_3 and Al_2O_3 can be found. Oxidation begins for group two in the same way as it does in group one, albeit group two has sufficient chromium in order to form an continuous sub-scale, aluminum is internally oxidized underneath this zone. Oxidation of group three is different to group one and two. While the start of the oxidation is similar, no further inner oxidation can be found in

the bulk of the material, due to the high content of aluminum. Now, it is possible for aluminum to form a continuous Al_2O_3 layer, which is formed right after NiO and Cr_2O_3 due to its lower growth kinetics.

Al_2O_3 does dominate the structure with rising temperature due to its greater thermodynamic stability [22,23]. This behavior can already be achieved if the composition has a 5 wt% aluminum and 5 wt% chromium concentration. Figure 13 displays a schematic drawing of the oxidation of group one to three.

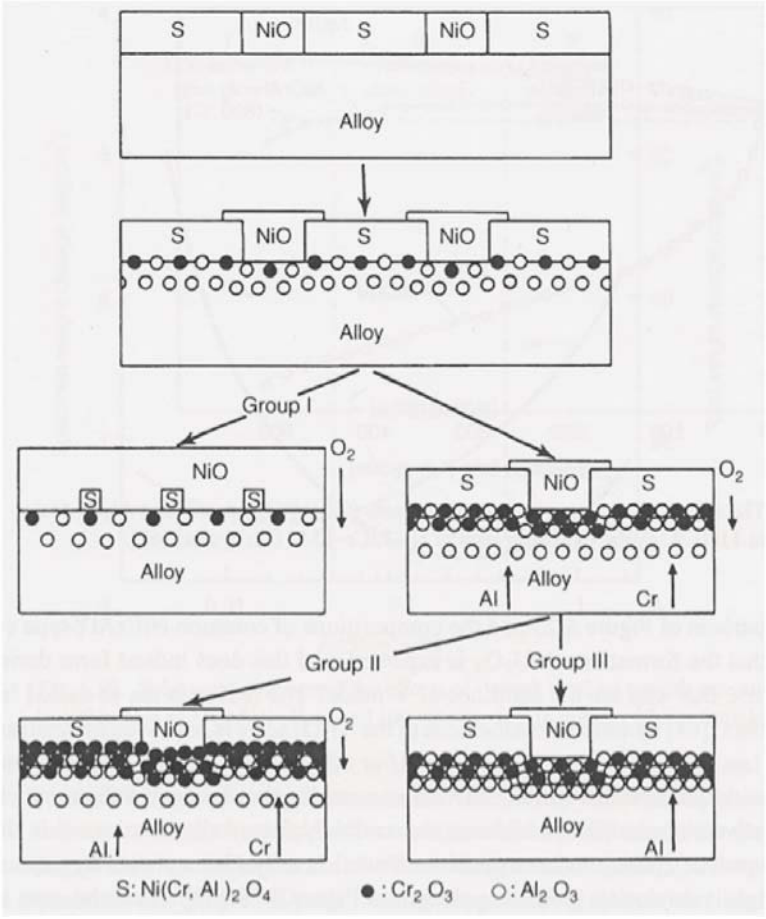

Figure 13 Schematic drawing of the oxidation mechanisms occurring in Ni-Cr-Al alloys [23]

1.2.2 Carburization of Metals

In many technical environments (CO, CO_2) and in atmospheres with high carbon activity at high temperatures, a protective oxide layer is not always possible to grow. Then carburization can occur. Two main cases of carburization can be defined [19, 21, 22, 23,25]:

CASE I: The carbon activity a_c is below one and a corrosive attack occurs due to internal carburization [25].

CASE II: The carbon activity a_c is above one and attack happens due to "metal dusting". This case does not play an important roll in the conducted experiments due to the lack of CO - H_2 [25].

CASE I: Internal carburization

The corrosve attack occurs via carbon penetration at the outer material layers, thus forming internal M_7C_3 and $M_{23}C_6$ carbides (M = Fe, Ni, Cr). The $M_{23}C_6$ carbides do have a lower energetic solubility product and are therefore first to diffuse, followed by M_7C_3 carbides. Those precipitates do change the mechanical properties of the material drastically:

(i) Loss of ductility
(ii) reduction of the melting point of the alloy
(iii) changes of microstructure due to extensive formation of chromium carbides
(iv) reduction of corrosion resistance due to loss of chromium

Internal carburization mainly occurs at high temperatures above 1000 °C and/or at low oxygen partial pressure (for below one), where it is impossible for the material to form a protective oxide layer. By adding silicium to the material, the effect of carburization can be minimized or completely stopped. Although an oxide layer prevents the carburization, it is possible, by poisoning the atmosphere and/or at temperatures above 1050 °C, that the protective oxidation layer fails [19, 22, 23, 25].

Diffusion kinetics of carbon in the tested materials can be defined using the diffusion classification of Harrison [26 27], which discusses three different diffusion patterns A, B, C (fig. 14) [27].

1. Type A kinetics are observed in limiting cases of high temperatures and/or at very long annealing times and/or small grain sizes. In such conditions the volume diffusion length, $(Dt)^{1/2}$, is greater than the spacing d between the grain boundaries and the volume diffusion fields around neighboring grain boundaries overlap each other [26]. Therefore the conditions can be defined as followed:

   $$(Dt)^{1/2} >> d \qquad (17)$$

2. Type B kinetics occur at low temperatures and/or short annealing times and/or the grain sizes are larger than in the previous case type A.

   $$s_{seg}\delta << (Dt)^{1/2} << d \qquad (18)$$

   s_{seg} defines the segregation quotient in the grain boundary, while δ is the width of the grain boundary. Grain boundary diffusion takes place at the same time as volume diffusion, but unlike type A, the diffusion fields of neighbouring grain boundaries do not overlap each other. Thus the solutions, used for insulated grain boundaries, are also valid for the polycrystal [26].

3. Type C kinetics starts right from the B regime, if lower temperatures and/or very short annealing times are present. This situation does lead to “freeze” all volume diffusion. A diffusion regime which takes only place along grain boundaries [26]:

   $$(Dt)^{1/2} << s_{seg}\delta \qquad (19)$$

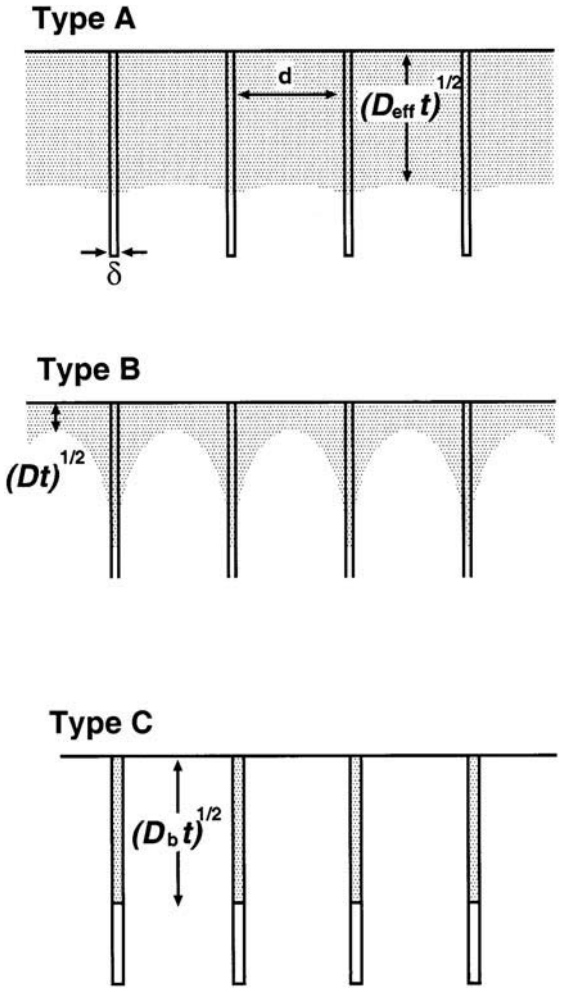

Figure 14 Schematic illustration of type A, B, and C diffusion kinetics according to Harrison classification [26].

The diffusion profiles shown above do follow a Gaussian function and the only quantity determined from the profile is D_{eff} the effective diffusion quotient. The Arrhenius plot shown in figure 17 describes the schematic diffusion patterns. At high temperatures, the lattice diffusion is dominant, while at lower temperatures and according to grain size, the grain boundary diffusion is becoming more and more the prominent diffusion conduct [21].

$$D_{eff} = D_V + \frac{\pi\delta}{d_G} * D_G \tag{20}$$

D_V denotes the volume diffusion quotient, while D_G stands for the diffusion quotient of the grain boundary. D_G equals the diameter of the average grain size.

The material is gaining weight due to the carburization process. This process follows the parabolic law; hence it is possible to define [21]:

$$s^2 = k_C^{'} * t \tag{21}$$

While all other parameters were explained earlier, in this case, $k_C^{'}$ denotes the carburization constant.

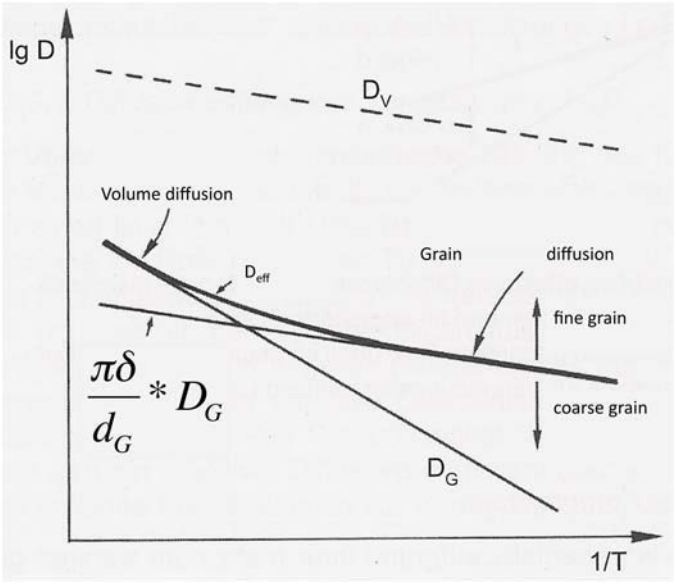

Figure 15 Arrhenius plot of the diffusion quotient depending on the temperature [23]. The dashed line signifies where the whole crystal activation energy equals the disolocation activation energy D_V.

2. Materials and Experimental Setup

To conduct the experimental studies of the behavior of carbon and oxygen, three materials were selected (table 1). H214 was chosen due to its high aluminum content; to increase the aluminum content even further H214 was aluminized (fig. 16). The material was annealed in 99 % Al powder for 1hour at 950 °C and later heat-treated at 1050 °C for 190 hours. The material was aluminized to achieve a direct comparison in the behavior of carbon and oxygen, corresponding to the aluminum content. The aluminum content was investigated using XRF. H1560 is a Ni based single crystal. Thus it can be utilized in comparison to the simulation, due to its ordered microstructure. The composition of the material was characterized using EDX. This allows the characterization of the impact of aluminum on the behavior of carbon and oxygen in such alloys at elevated temperatures.

Table 1 Chemical composition in weight percent of H214, H214Al and H1560.

Material	Ni	Cr	Al	Fe	Mn	Si	Co	C	B	Y	Cu	Ti	Ta
H214	75	16	**4.5**	3	0.5	0.2	0.1	0.05	0.01	0.01	0	0	0
H214Al	76.5	12.3	**9.36**	1.51	0.15	0.04	0.1	0.04	0	0	0	0	0
H1560	68.25	5	**20**	0	0	1	3	0	0	0,25	1	0.5	1

The element's behavior was tested at the temperature of 750 °C for 1000 hours and at 1000 °C for 24 hours; during this time the samples were exposed to air or graphite (table 2). The experimental setup was chosen due to the higher and lower end of the temperature range a turbine blade might be exposed to, while the timeframe is adjusted to an area usually used for high temperature experiments.

Table 2 Test configurations of the materials, while exposed to air or graphite coating

Exposure time [h]	Exposure Temperature [°C]	
	750	1000
24		H214 H214Al H1560
1000	H214 H214Al H1560	

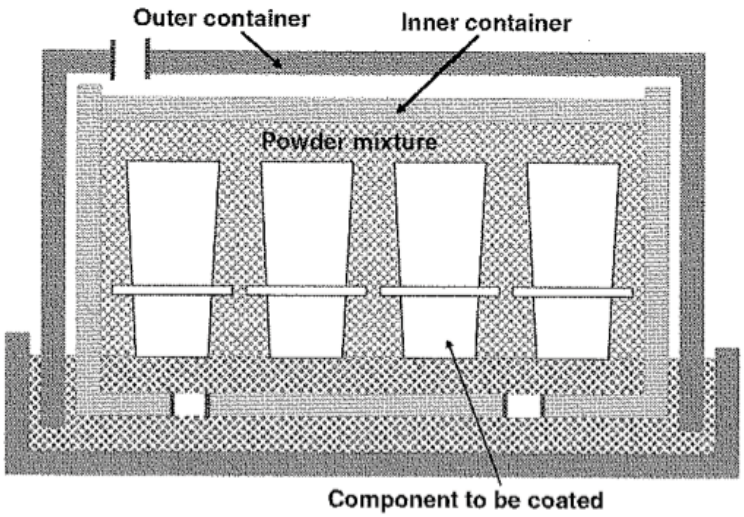

Figure 16 Schematic diagram of an apparatus used for aluminizing by pack cementation. [22]

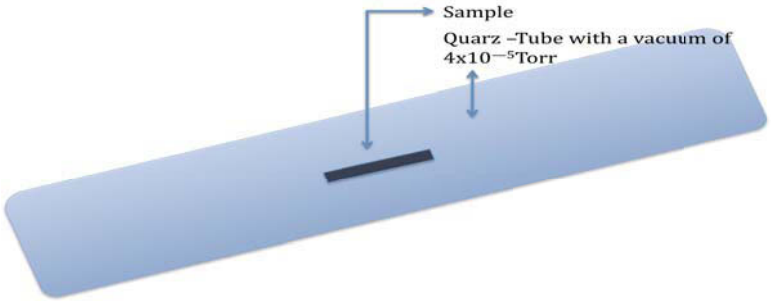

Figure 17 Quartz-Tube with a sample and a vacuum of $4x10^{-5}$Torr. The sample is positioned horizontally in the tube, which is further ordered horizontally in the furnace.

All samples were polished to a surface roughness of 0.25 µm. The samples selected for the carburization experiment were then coated with a graphite spray and encapsulated in quartz at a vacuum of $4x10^{-5}$ Torr (fig. 17). The average thickness of the graphite coating was determined by characterization of a sample by using SEM. The thickness of the coating was 13 ±1.5 µm.

Then samples were embedded in Epoxy and coated with a 20 nm thick conductive layer. To observe the grain-boundaries and the γ/γ' interface, the samples were etched in an acid consisting of 33 % water, 33 % acetic acid (CH_3COOH), 33 % nitric acid (HNO_3) and 1 % hydrofluoric acid. The samples had to be etched for up to 30 minutes. To characterize the samples, various instruments were used, such as an optical microscope, an Inspect F scanning electron microscope, a Helios focused ion beam microscope and an EDX analysis.

The following tables present data regarding some fundamental properties of the materials, which are necessary in order to characterize and to perform an analysis relevant for the obtained data.

Table 3 provides density and melting temperatures of oxides, which are going to be encountered, while table 4 provides useful information pertaining to the diffusion data obtained by literature research.

Table 3 Density and melting temperature of chosen oxides [24].

Oxide	Al_2O_3	Cr_2O_3	NiO
ρ [g/cm³]	3.9	5.2	6.6
T_M [°C]	2053	5435	1990

Table 4 Diffusion data of chosen materials

Material (Matrix, Solitude)	D_0 [cm²/sec]	Q [eV]	T [°C]
Cr, C [28]	3 - 9	1-149	1200 - 1500
Ni, C [29,30]	3 - 7	1.69 1.62	1000
Ni_3Al, Ni [31]		3.09 3	770 - 1357

3. Results

3.1 Simulation Results

The lattice parameters for pure elements are often well known, unlike those for multi-component systems. In order to achieve accurate and fast calculations, these values are of outermost significance as well as the KPOINTS and ECUT values. The KPOINTS and ECUT can already be determined by systems for pure elements, which saves time. In a multi-component system, the ECUT is usually chosen from the highest ECUT value from all elements in the system and then increase by 25 %. The KPOINTS are not altered as long as the system size remains. The cohesive energy, equilibrium lattice constant, and bulk modulus are determined by fitting the energy versus volume data to a Birch polynomial [32]. Considered were the following additional impurities in our calculations: C, O, Cl, N. To obtain the energy change those elements introduce into the system, the point defect energy per atom has to be calculated:

$$E_F = E - \left(\frac{x}{n} E_{Ni} + \frac{1-x}{n} E_{Al} \right) - E_I \qquad (22)$$

E is the total energy of a system with a point defect, E_{Ni} is the free formation energy of nickel while E_{Al} is the free formation energy of aluminum and E_I denotes the free formation energy of an interstitial element. n denotes the sum of nickel and aluminum atoms in a system. As a result E_F is the difference between a system with point defect and a pure systems, the free formation energy.

The data provided in table 5 are used to calculate the free formation energy and the point defect formation energy for this thesis. Therefore the data should be available for further investigations of similar problems as well as for comparison studies.

Table 5 Energies of pure systems in various super cell configurations and the free energy formation for a single atom.

Elements	E [eV]	E_F per atom [eV]
Ni	-176.4502	-5.5141
Al	-119.7507	-3.7422
C	-3.5443	-1.7722
Cl	-16.6287	-8.3144
N	-9.8784	-4.9392
O	-122.7560	-3.8361

As a first step, the equilibrium of pure Ni_3Al (γ') and Ni (γ) was calculated. An interstitial impurity was later added to the system and calculated (table 5). Ni_3Al has a L12 structure with octahedral Ni-rich, octahedral Al-rich, and tetrahedral interstitial sites. The possible location sites are shown on a Ni_3Al unit cell in figure 18.

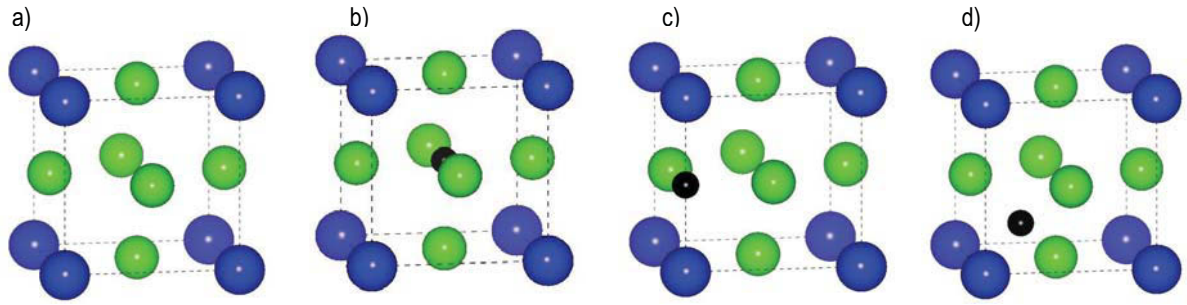

Figure 18: Possible interstitial lattice sites from left to right,
a) a Ni_3Al unitcell without an interstitial element aluminum atoms are blue, while nickel atoms are green
b) Carbon (black) on a nickel rich octahedral position
c) Carbon on an aluminum rich octahedral position
d) Carbon on an tetrahedral position

Initially, the point defect formation energy per atom for Carbon and Oxygen in a pure Ni single crystal was calculated (fig. 18). The calculated results presented below allow a first prediction. Oxygen has a higher affinity to pure nickel than carbon. The different lattice position for oxygen is not as significant as in the case of carbon, because there is only a difference of 0.003 [eV] per atom between the lattice sites. In contrast, carbon does have a difference of 0.037 [eV] per atom between a tetrahedral and an octahedral position.

The negative formation energy value (fig. 19) indicates that the reactions of the interstitial elements (O and C) might be spontaneously; therefore it might be beneficial for the formation energy of the system. A system is always driven by its need to achieve the most stable energetic formation, which is considered as the lowest energy level.

While in a pure Ni-system, the distinction between the elements might be minor; the difference for Ni_3Al is more pronounced (fig. 20). The point defect formation energies are positive, which suggests that energy must enter into the system to induce an interstitial atom. The atom is forced into the crystal lattice, reducing the stability of the formation. Hence, increasing the total system energy induces a less stable structure.

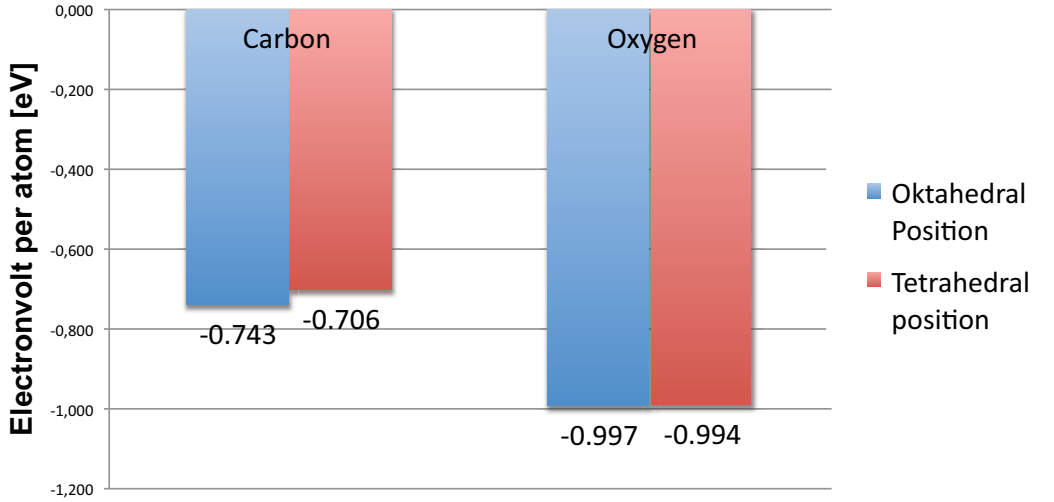

Figure 19 Point defect formation energy per atom of a 3x3x3 super-cell for a pure Ni system. Note that the energy does not differ too severely between octahedral and tetrahedral position.

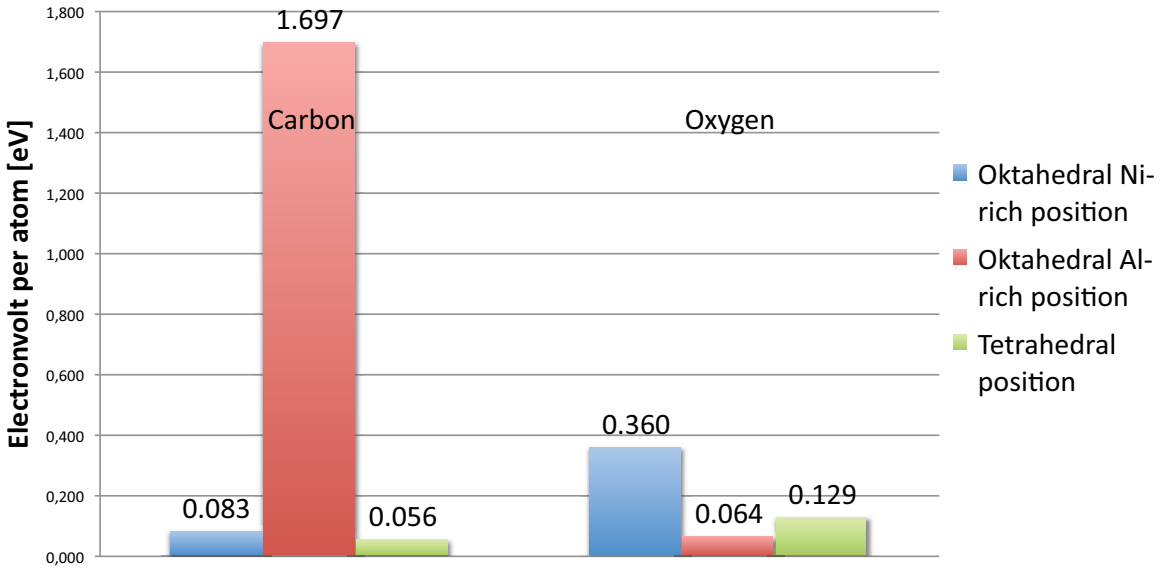

Figure 20 Point defect formation energy per atom of a 3x3x3 Ni_3Al super-cell. Note the increase of energy necessary for a carbon atom to occupy an aluminum rich octahedral position.

The values obtained by the simulation indicate that carbon prefers a Nickel rich area compared to an aluminum rich lattice site position. The energy of 1.697 [eV] is required to force a carbon atom close to an aluminum rich lattice site. This is a huge amount of energy, indicating that carbon is trying to avoid any aluminum rich lattice site positions. Oxygen on the other hand, shows a huge affinity to aluminum, which results in the lowest point defect formation energy at an aluminum rich position or a lattice site close to aluminum.

During the experiment, oxygen is drawn to Aluminum in order to form an Al_2O_3 layer while Carbon is trying to avoid Aluminum rich positions. For a Ni, Ni_3Al interface Carbon is more likely to be found in the nickel phase well aligned to the cubic orientation of the system, instead of entering the Ni_3Al phase. Oxygen, on the other hand, will head straight for the aluminum rich γ' phase, which will conclude in oxidation of the Ni_3Al phase, yet results in an aluminum oxide layer which prohibits further oxidation of the material.

According to the point defect formation energies, it is possible to predict the diffusion paths of the simulated interstitial elements. An octahedral - octahedral diffusion (O-O pathway) (fig. 21), or a tetrahedral – tetrahedral (fig 22), T-T pathway, is unlikely to be performed in this case. If a carbon atom would perform a jump from an aluminum rich position towards another aluminum rich position inside a Ni_3Al phase, it is more likely to see octahedral – tetrahedral – octahedral diffusion pathway (O-T-O diffusion) (fig. 23). The pathways displayed below (fig. 21-25) represent possible pathways in a perfect structured material while a crystal with defects inside tend to establish pipe diffusion, which is essentially a diffusion path for elements similar to grain boundaries inside a crystal.

It must be noted that while calculating the T-T diffusion pathway and the O-T diffusion pathway displayed in figure 21 and figure 22, a spring constant mistake occurred which had no effects on the result of the calculation, but conclude in a downslide of the two data - points.

The possible diffusion paths for carbon and oxygen are displayed below in figures 24 and 25. While there are no huge differences in the diffusion path of the interstitial elements in a pure nickel structure [30], it is quite different for a Ni_3Al structure (fig.24). As mentioned earlier carbon is going to avoid aluminum rich positions, while oxygen is favoring those. Figure 24 and figure 25 display estimated diffusion paths for carbon and oxygen in a Ni_3Al system. Evident in figure 21 (which displays an O-O diffusion path), the activation barrier energy is not located at the middle of the diffusion path, though rather at locations where the atom is forced to squeeze itself past the atoms of the system. Those peaks are missing in the estimated pathways for carbon and oxygen corresponding to the fact that the calculation was not possible due to limitations in the computational opportunities. Displayed further are two different diffusion types, a tetrahedral-tetrahedral jump (fig. 22) and an octahedral-tetrahedral jump (fig. 23).

Further the point defect formation energies for Chloride and Nitrogen were calculated (fig. 26 and fig. 27). It is obvious that the interstitial elements prefer to be close to aluminum (nitrogen in particular), indicated by the aluminum-rich tetrahedral position. The interstitial elements are going to avoid nickel–rich and rather go for the aluminum rich phases in the material.

The other possible positions for the interstitial elements need a huge amount of energy to be forced at the specified lattice site and are therefore more unlikely to occur. The additional energy put into the system also increases the system energy, which leads to a more unstable system configuration and is therefore not preferred.

Although the influence of wide and low angle grain boundaries as well as coherent interfaces is not considered in the simulation results, there is a certainty that the elements are behaving as calculated in an environment closely related to a bulk system. It is therefore safe to consider the same assumptions for the diffusion paths for chloride and nitrogen as for carbon and oxygen. Results are summarized in tables 6 to 8.

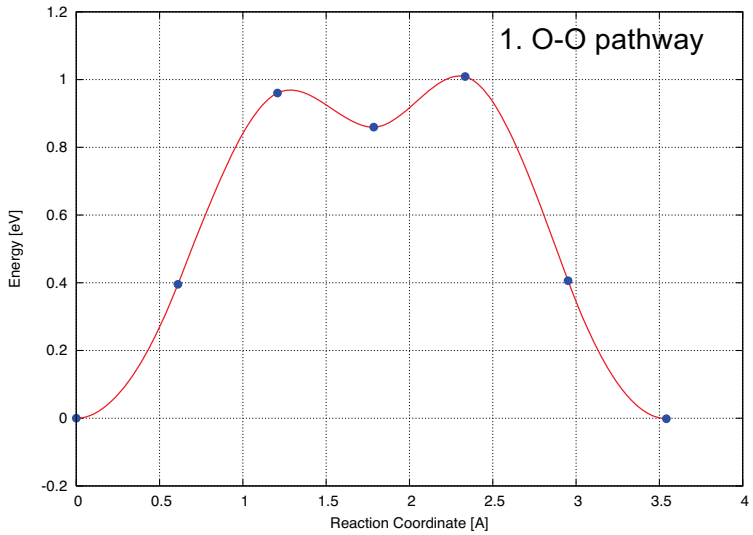

Figure 21 Octahedral-Octahedral diffusion path for a carbon atom in a Ni_3Al cell.

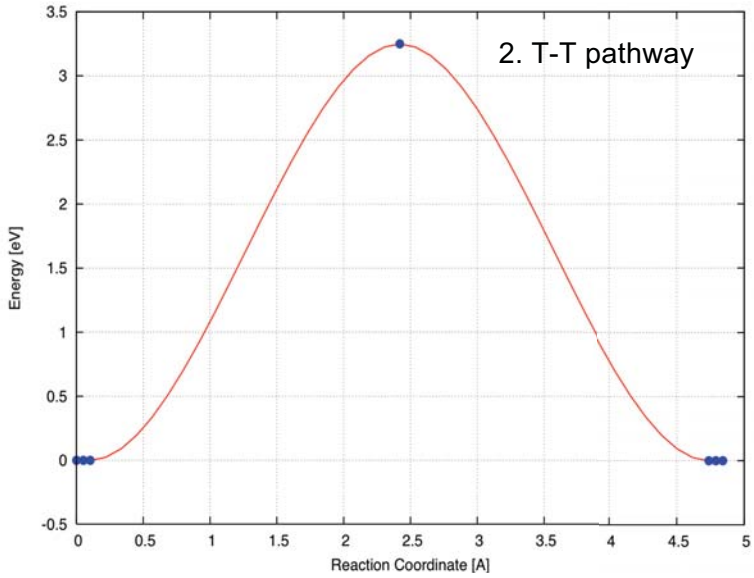

Figure 22 Tetrahedral-Tetrahedral pathway of a carbon atom in Ni_3Al cell. Note the amount energy necessary for carbon to be able to jump to the next tetrahedral lattice site position.

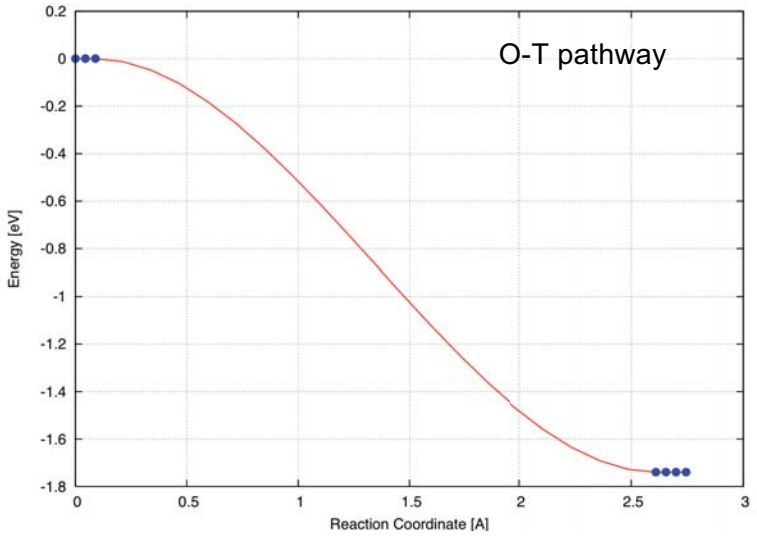

Figure 23 Octahedral aluminum rich to a tetrahedral diffusion path for carbon in Ni_3Al. The diffusion path suggests that it is more likely for carbon to be found in the tetrahedral position, which is energetically more stable than the aluminum rich octahedral position.

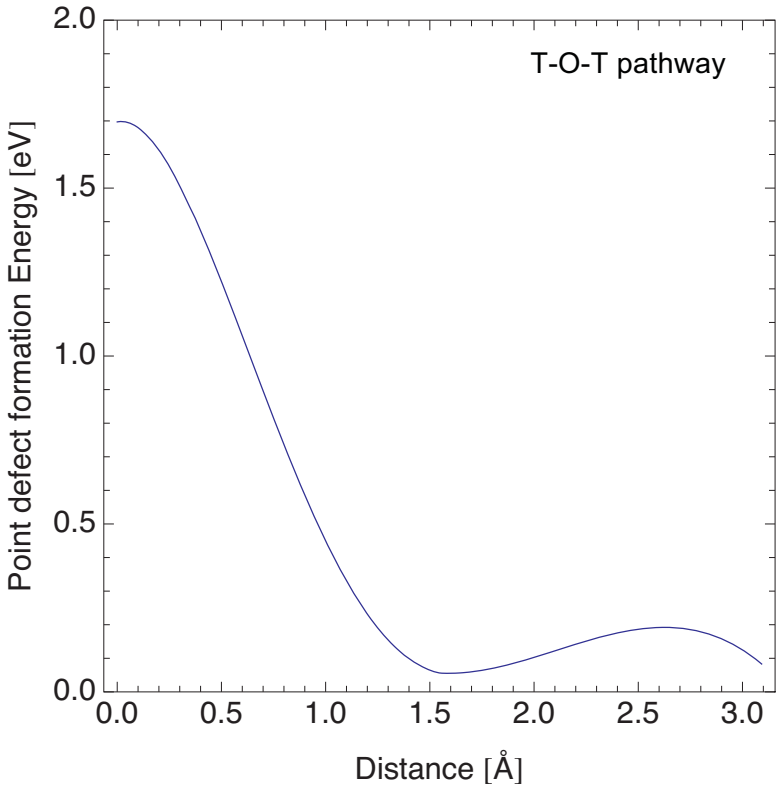

Figure 24 Estimated octahedral – tetrahedral – octahedral diffusion pathway of a carbon atom in a Ni_3Al structure.

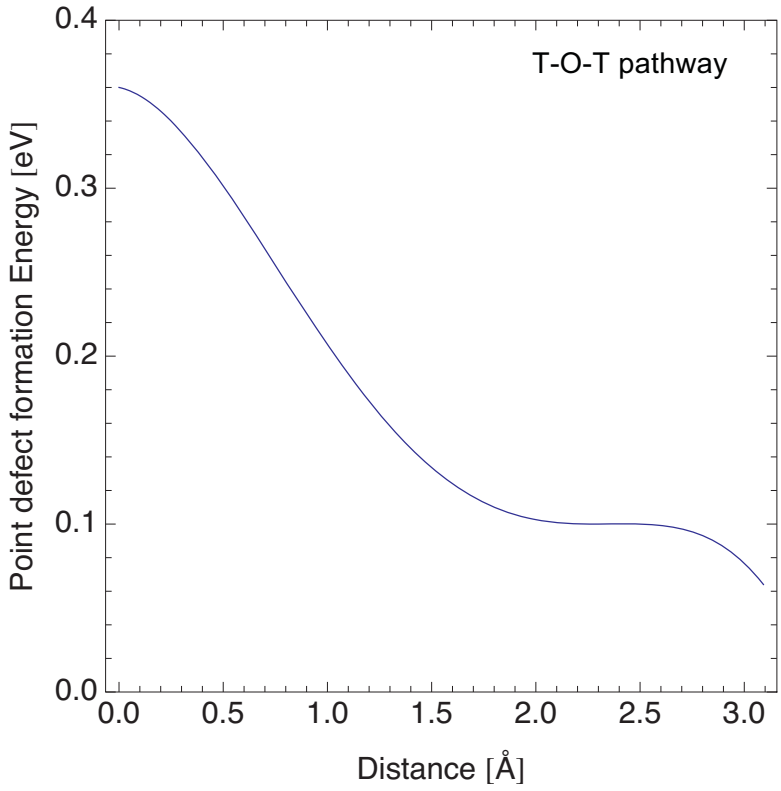

Figure 25 Estimated octahedral – tetrahedral – octahedral diffusion pathway of an oxygen atom in a Ni_3Al structure.

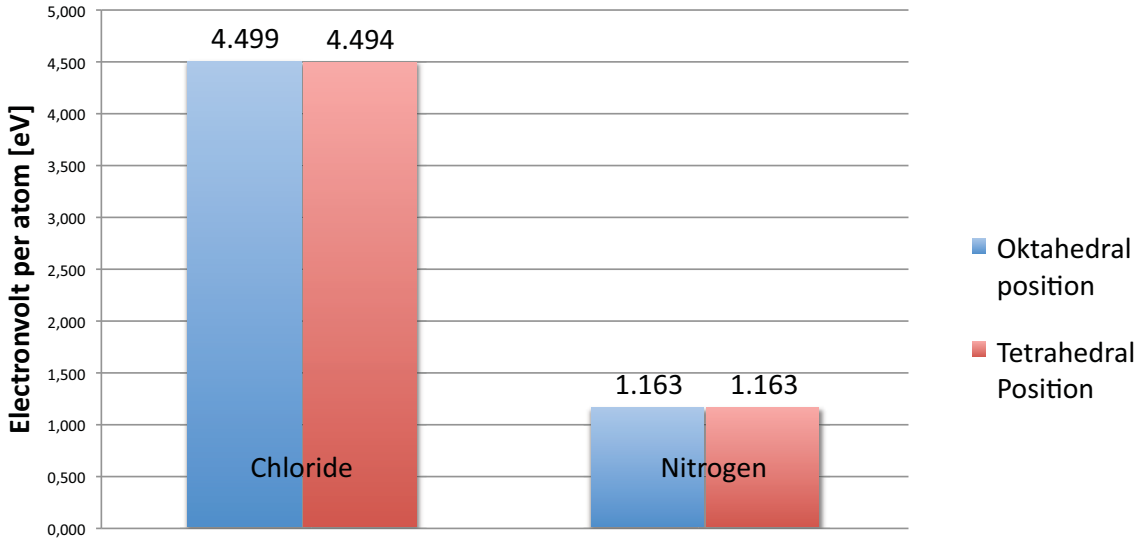

Figure 26 Displayed is the point defect energy for a pure 2x2x2 nickel super-cell with different interstitial atoms at different lattice site locations.

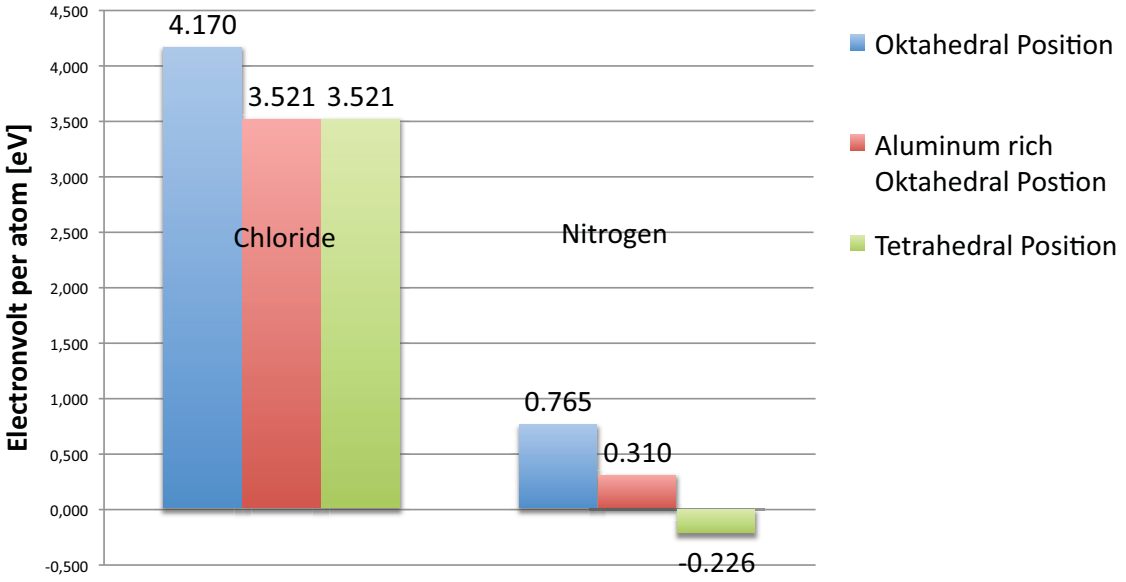

Figure 27 Displayed is the point defect formation energy for chloride and nitrogen in a 2x2x2 Ni_3Al super-cell. According to the obtained results above chloride is going to avoid aluminum at all costs, while nitrogen seems to achieve a stabilized position in a Ni_3Al system.

Table 6 Point defect energy for a pure nickel system

Material	Point defect energy [eV]		Point defect energy per atom [eV]	
	octahedral	tetrahedral	octahedral	tetrahedral
C	-610.946	-610.909	-5.605	-5.605
Cl	-174.727	-174.733	-5.295	-5.295
N	-184.607	-184.606	-5.594	-5.594
O	-607.052	-606.863	-5.569	-5.568

Table 7 Point defect energy for a Ni_3Al system

Material	Point defect energy [eV]			Point defect energy per atom [eV]		
	octahedral1	octahedral2	tetrahedral	octahedral1	octahedral2	tetrahedral
C	-609.533	-607.918	-607.917	-5.592	-5.577	-5.577
Cl	-175.057	-175.706	-175.705	-5.305	-5.324	-5.324
N	-185.004	-185.459	-185.995	-5.606	-5.620	-5.636
O	-605.107	-605.402	-605.338	-5.551	-5.554	-5.554

Table 8 Activation energy necessary for a diffusion jump in a Ni_3Al system for various diffusion paths

Diffusion path	Q [eV]
octahedral - octahedral	1.011
tetrahedral - tetrahedral	3.347
tetrahedral - octahedral	1.614

3.2 Experimental Results

3.2.1 High Temperature Exposure to Air

H214

As observed from the simulation, oxygen has a high affinity to pure nickel besides a preference for aluminum reach positions. It was therefore expected to see a well-defined reaction of the material towards oxygen. Additionally, it is known that oxygen is forming stable aluminum and chromium oxide layers. Those layers do protect the material from further oxidation due to their dense nature. It was observed that Ni formed a layer of nickel oxide. After forming this first diffusion barrier, the diffusion of oxygen was slowed down, as it had to penetrate the nickel oxide layer first. It then diffused deeper into the material, hitting aluminum and chromium atoms and forming a second oxide layer of aluminum and chromium oxides inside the material (fig. 28). Figure 28 displays a cross section of H214 annealed at 750 °C for 1000 h. It shows the various ranges of oxidation, the material suffered. Area one displays the unaltered bulk material, while area two shows a chromium richer zone as well as a Kirkendall effect caused by the diffusion of nickel (arrow). Area 3 is a nickel oxide layer in which aluminum oxide can be found as well. Judging from fig. 28, it is not entirely possible to define which element occupies certain areas therefore elemental maps allow to visualize the diffusion process better (fig. 29).

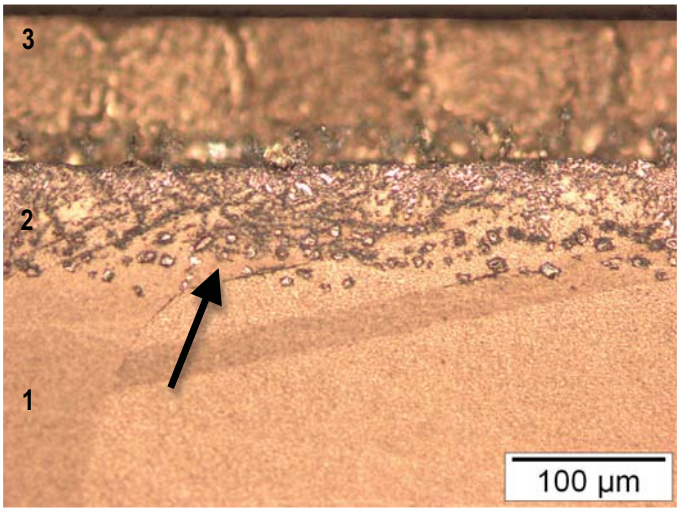

Figure 28 H214 annealed at 750 °C for 1000 hours at air. Three areas can be observed. Area (1) the unaffected bulk material, area (2) displays the inner oxide scale while area (3) shows the outer oxide scale.

In fig. 28 a Kirkendall effect (arrow) can be observed, which is caused by the fast diffusion of nickel towards the nickel depleted areas close to the surface caused by oxidation. This observation is later confirmed using a line scan. The lack of further chromium would have compelled to an advance of the nickel oxide layer embedded with $NiCr_2O_4$ precipitates and resulted in an oxidation of chromium inside the material. In the case of H214 and H214Al, aluminum as the third main alloying element, prevents an inner oxidation by forming an Al_2O_3 layer, therefore effectively stopping the corrosion of the material.

Figure 29 displays elemental maps taken of the sample. Note the thick aluminum layer towards the surface; while it seems that, despite the aluminum concentration on the surface is much higher than in the bulk, there seems to be no gaps of aluminum. The thick layer of oxygen (indicated by the oxygen distribution) is marked. The oxygen concentration is later decreasing towards the deeper regions into the bulk. Due to the fact that oxygen is rather difficult to detect and that there is high oxygen background detection, the oxygen shown in area two can be considered a background fragment (area I.(a)). The behavior of aluminum can be explained by its rather slow oxide growth compared to nickel and chromium oxides.

The behavior of chromium and nickel are also well displayed. While chromium is evenly distributed throughout the material, its density at the surface is much lower in area III.(a) a than in the other bulk material and it appears to create chromium depletion in area III.(b) by diffusing faster towards the reactive zone, forming Cr_2O_3, than the bulk can reoccupy the empty lattice sites. As mentioned earlier, nickel oxides do have a much higher growth kinetics and therefore NiO is formed faster than oxides, which leads to further diffusion of nickel towards the surface, than it could diffuse from the bulk to the nickel depleted region. Therefore a Kirkendall effect occurred, which is visible with the optical microscope in conjunction with the EDX characterization.

The line scan (fig. 30) also unveils how deep the material is affected by the rapid diffusion of nickel and chromium towards to the surface. It illustrates the elemental distribution inside the material. While all changes are happening in the first 150 µm of the bulk, the rest of the material seems unaffected by any changes caused by diffusion. Overall, there are two different oxide layers; the first consists mainly of nickel and chromium oxide while the main components of the second layer are chromium and aluminum oxides. The nickel oxide layer as well as the aluminum and chromium oxide layer is clearly marked in fig. 30 (area 1 - red circle). Furthermore the nickel depleted area, which is caused by the Kirkendall effect, can be easily identified (area 2 - blue cicle).

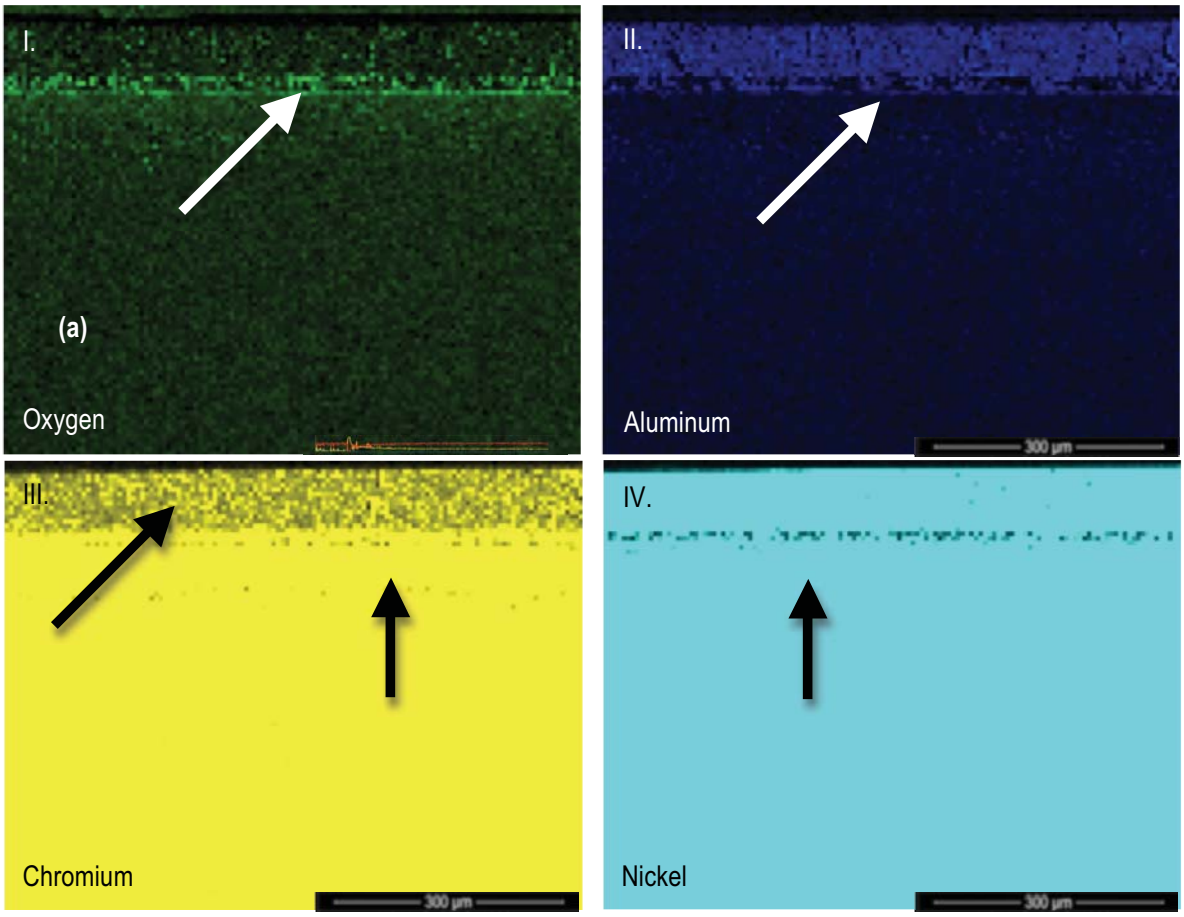

Figure 29 Elemental map of aluminum in H214 exposed to air at 750 °C for 24 hours. A well-defined aluminum scale (II) can be seen together with chromium oxide (III). The formation of NiO (IV) resulted in nickel-depleted areas inside the material (arrow), Kirkendall effect. The elemental map of oxygen (I) has to be regarded carefully due to influence of the background.

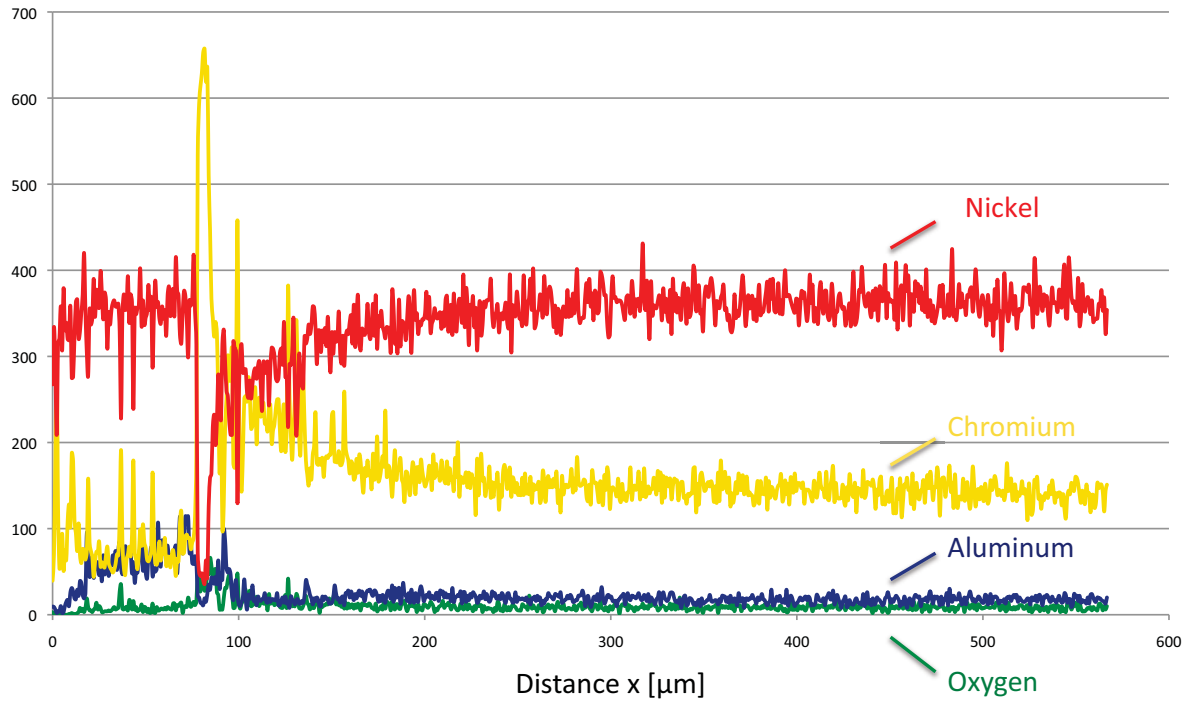

Figure 30 Displayed is the results of the EDX line – scan for H214 annealed in air at 750 °C for 1000 h. Clearly visible are the different oxide scales as well as the chromium and nickel depleted areas further inside the material.

H214Al

While in H214, the Kirkendall effect was obviously easily allocated to one element, visible on Figure 28 and figure 29; it posed a challenge to determine it in H214Al. Allegedly, on the elemental maps (fig. 31), the Kirkendall effect does occur. The oxide layer of H214Al is more complex than that of H214. There is already a high content of chromium in the first oxide layer. The chromium content is increasing, while nickel and aluminum are on a regional low (fig. 31). The bulk material of H214Al is affected to 200 µm below the surface (fig. 32). The line-scan further unveils different oxidation layers of the material, which occurred due to the heat treatment. As seen earlier, distinct patterns of nickel, aluminum and chromium are visible. Nickel and chromium depleted areas can be seen. Those areas are caused by the formation of NiO and Cr_2O_3. Chromium acts as an oxygen getter and protects the bulk material from further oxidation.

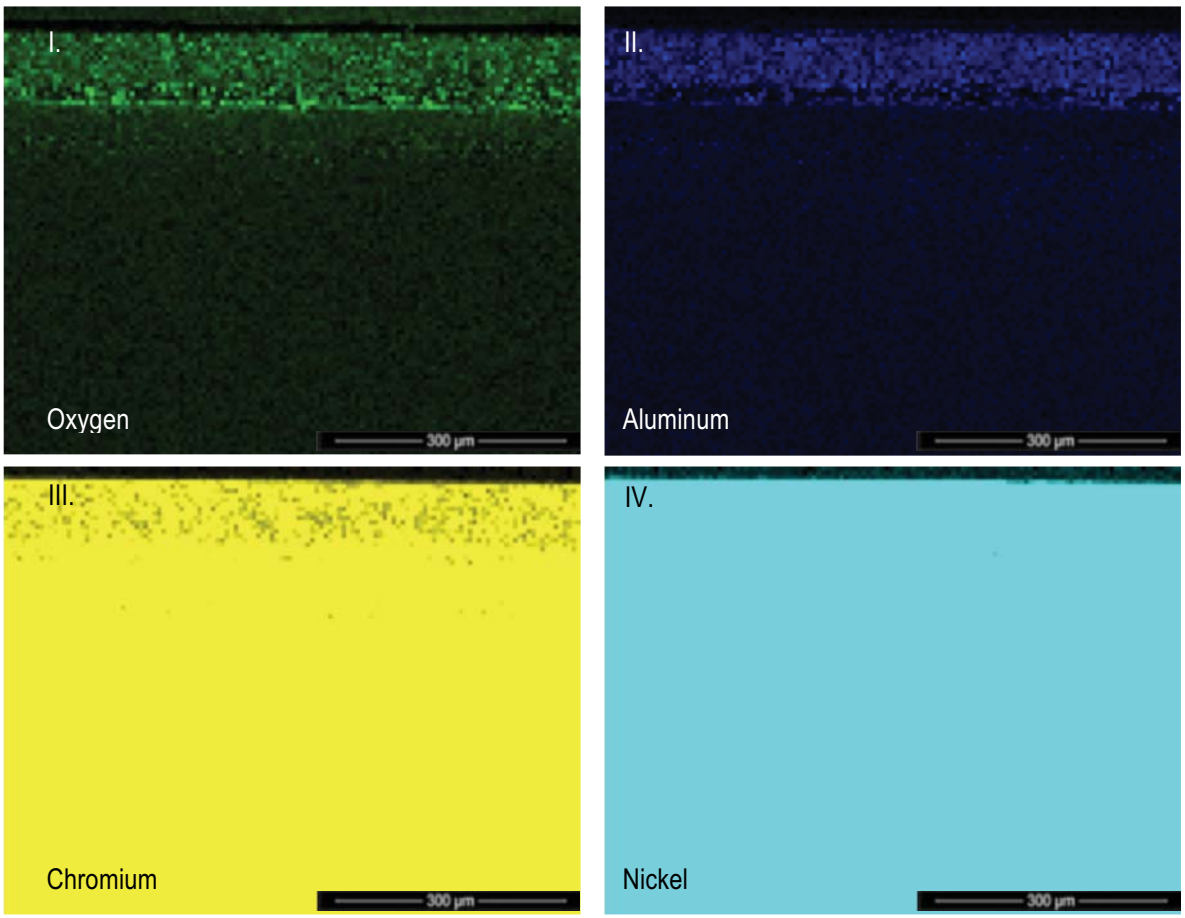

Figure 31 Element maps of H214 annealed in air at 750 °C for 1000 h. The oxide front (I), the aluminum oxide (II) and the chromium layer (III) are clearly visible. Nickel (IV) on the other hand seems not to be as severe affected as before.

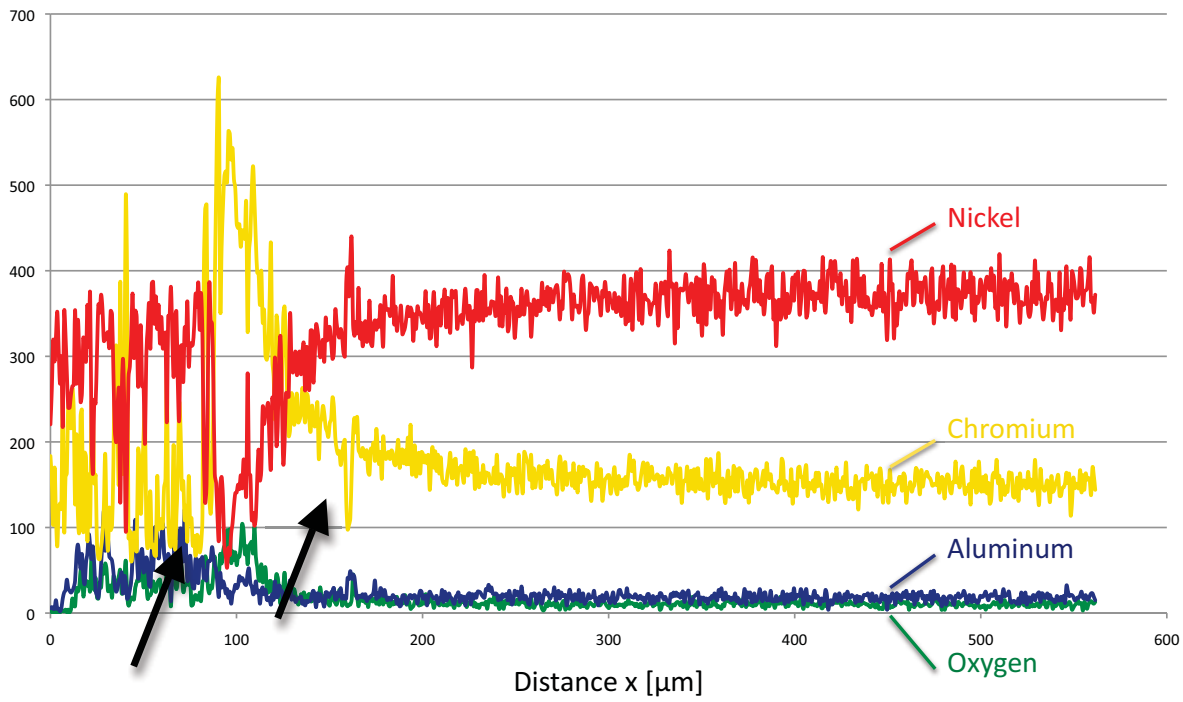

Figure 32 Line-scan taken of H214Al annealed in air at 750 °C for 1000 h. Noteworthy are the peaks displayed in the line-scan, which occur roughly at the same time as depleted areas (marked) do occur. Each time nickel and aluminum decrease the chromium concentration is peaking.

H1560

In H1560, oxygen has a similar effect on the material as on the other materials at a testing time of 1000 hours at 750 °C (fig. 33). Similar to previous samples exposed to air, the sample showed an affected area with a wide spread of an even more distinct diffusion front. The outer nickel oxide layer and the aluminum and chromium rich oxide layers below are clearly visible (fig. 33 marked and fig 34). The advance of oxygen is clearly indicated in the first picture in addition to the slow decrease of the oxygen level as well as the reactions of the materials towards the advancing oxygen. Ni_3Al or γ' does react unstable to the advance of oxygen, which would agree with the simulation results. The simulations suggest that oxygen would be more stable in Ni_3Al or in an aluminum rich environment [23].

$$2Ni_3Al + \frac{3}{2}O_2 \rightarrow Al_2O_3 + 6Ni \qquad (23)$$

While nickel forms a NiO layer, it leaves a nickel depleted layer behind which is then occupied by chromium and aluminum, which form a better layer and hinder the oxygen to advance further into the material (fig. 34).

The depth of the affected zone can also be seen by a line-scan (fig. 35). The oxidation front is clearly visible as well as the broad areas of aluminum and chromium oxides. The characteristics of the two oxide layers are clearly visible. In the first 20 - 30 µm, a porous nickel oxide layer is located; the second, denser aluminum and chromium oxide layer starting at around 30 µm. The material is affected to a depth of at least 80 µm by the diffusion of oxygen into the system. This is - compared to the other materials - rather shallow, which is quite well. As observed before, oxygen diffused to a depth of around 150 µm.

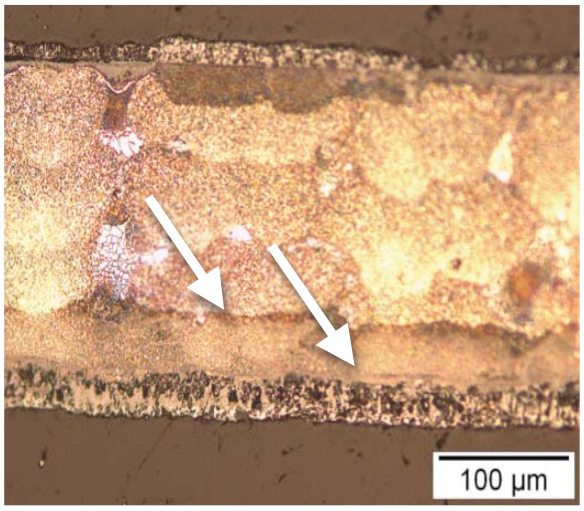

Figure 33 H1560 annealed in air at 750 °C for 1000 hours at air. Note the differences in the oxidation layers, which can already be clearly distinguished by the coloring of the material.

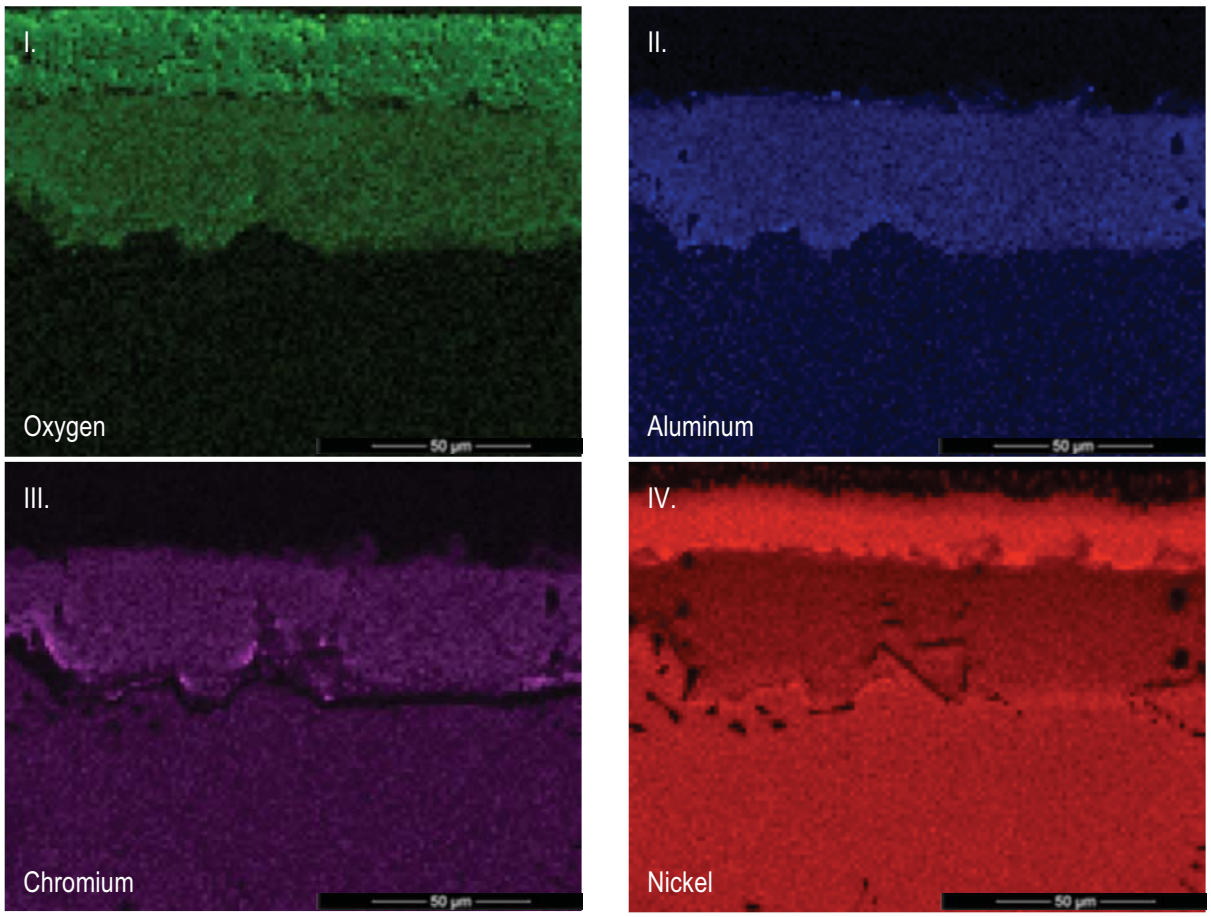

Figure 34 Elemental map of H1560 are ordered as followed; Oxygen (I), Aluminum (II), Chromium (III) and Nickel (IV). The diffusion front of oxygen can be seen corresponding to the oxide scale growth of the other materials. The advancing NiO and its nickel depleted hinterland are distinguished

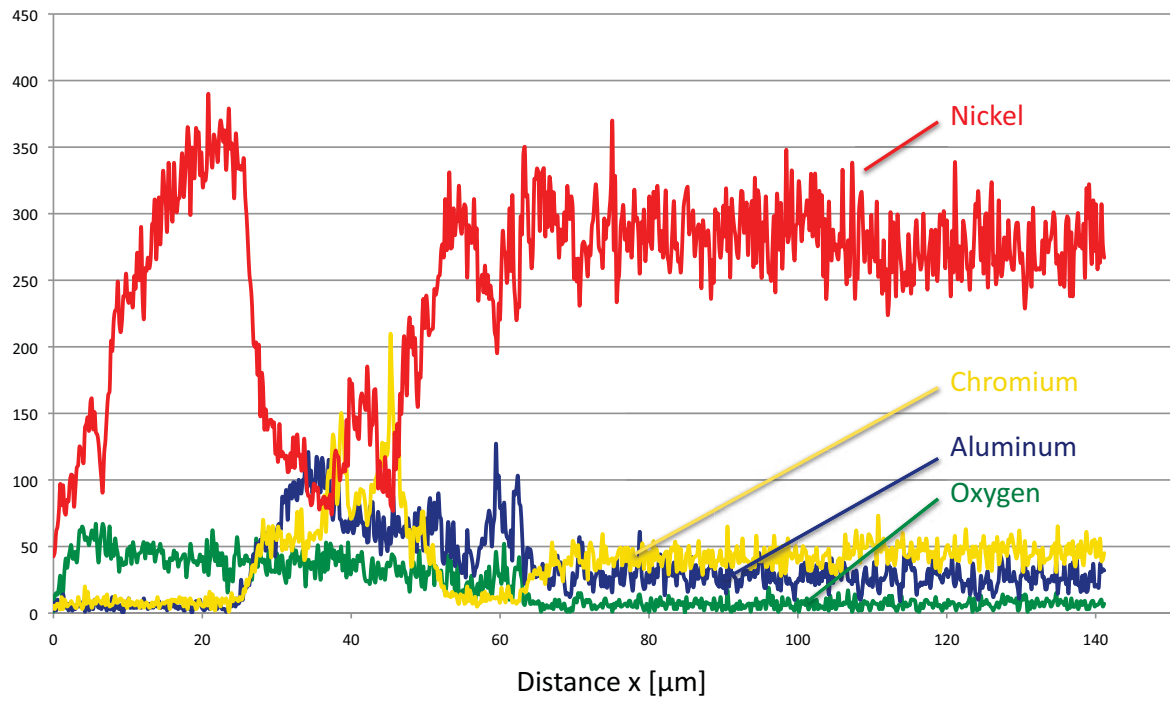

Figure 35 Line-scan of H1560 annealed in air at 750 °C for 1000 hours at air. The characteristics of the two oxide layers are clearly visible. In the first 20 µm a porous nickel oxide layer is located; while the oxide scale in the hinterland consists of aluminum and chromium oxide. The material is affected to a depth of at least 80 µm by the diffusion of oxygen into the system. This is - compared to the other materials - rather shallow. As observed earlier where oxygen diffused to a depth of around 150 µm.

The oxide layers were characterized using FIB in STEM mode, to achieve a precise data collection. The material for the STEM foil was cut from an area with a predefined oxidation layer (fig. 35). To avoid damage to the sample, its surface was coated with carbon. To delineate it, an ion beam was used afterwards. In the bulk material the typical microstructure of a nickel single crystal material can be seen.

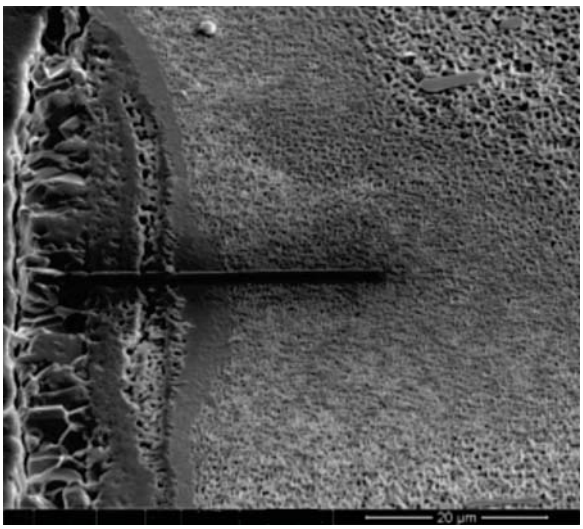

Figure 36 Area of H1560 (750 °C, 1000 h). Displayed is the selected area for STEM characterization.

The different areas one to four (fig. 37) on the STEM foil of H1560 were later characterized with the energy dispersive X-ray diffraction. Those are 4 main stages; the numbers mark areas in the bulk material which, depending on their state of oxidation, are visible starting from the bulk material to the surface (right to left). While the first stage shows no influence of oxygen and displays an ordered Ni-matrix and Ni_3Al bulk system, stage 2 displays already first signs of oxidation. The Ni_3Al phases are dissolving and losing their 001 orientation due to the increasing misfit, are yet still recognizable. Afterwards the phase is unrecognizable from the rest of the matrix. This results from the fast diffusion of nickel towards the surface and the high affinity of aluminum towards oxygen forming Al_2O_3. Further reasons are: the high affinity of chromium to oxygen forming Cr_2O_3 and therefore together with aluminum forming the “getter” layer (fig. 37). The oxide layer on the last displayed area is a nickel - oxygen layer. This layer has already suffered severe damage due to oxidation and appears porous, when examined via FIB in STEM mode.

Area three was characterization of H1560 using EDAX methods to receive a chemical composition of this severely affected zone. This characterization serves the purpose to have an improved knowledge of the surface region in order to be able to produce an accurate model. The data obtained can be seen in fig. 38 and table 9. Note that high concentrations of carbon and silicon are measured, which do not represent the actual concentrations of the elements in the materials but can be explained as background artifacts.

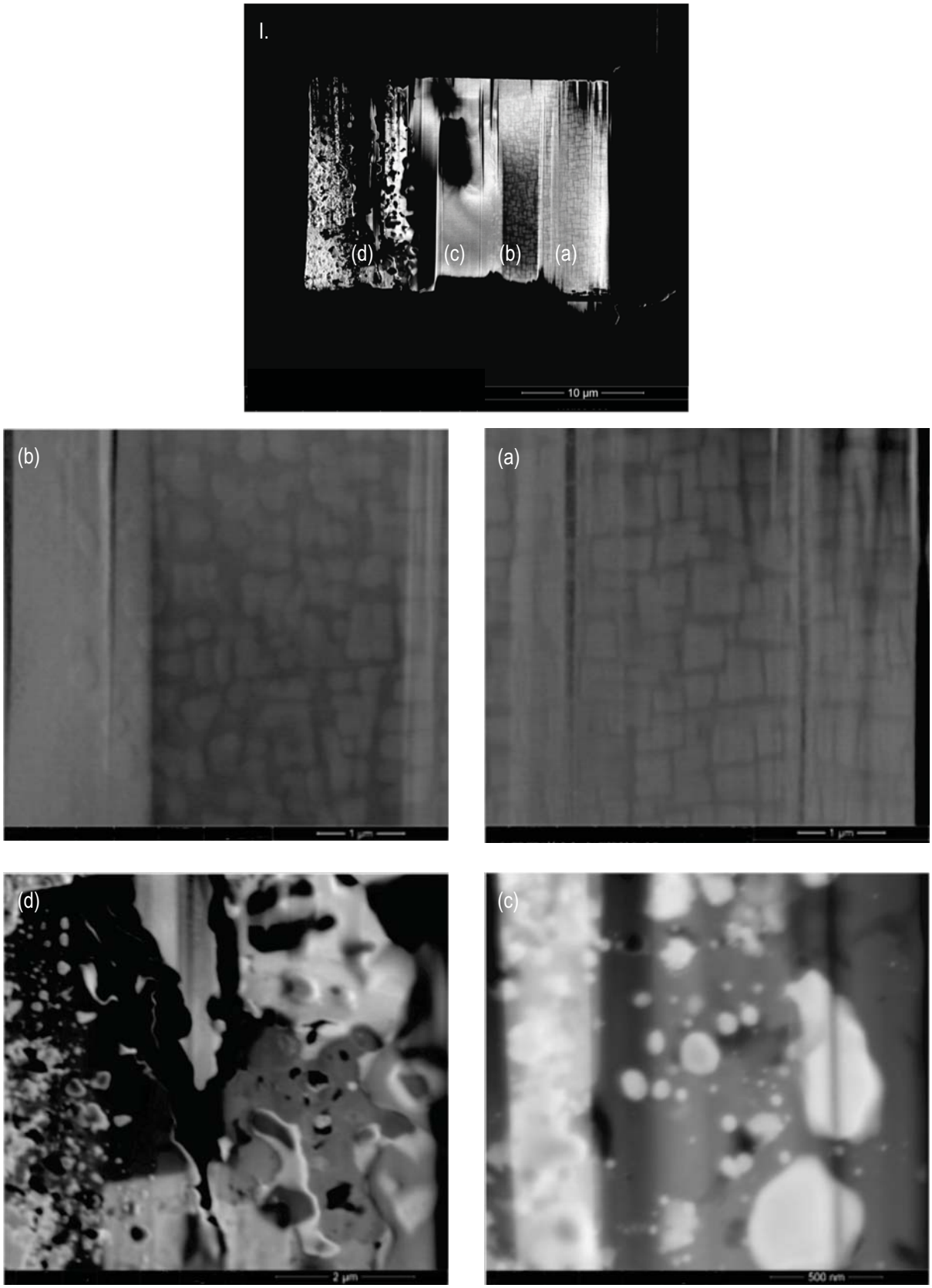

Figure 37 STEM foil of H1560 (I) displaying different stages of oxidation. The numbers do mark areas in the bulk material depending on their state of oxidation. Area (a) of H1560 is magnified on the right hand side. It can be clearly seen that the microstructure is not yet affected by oxygen. Areas (b) to (d), do show the stages of oxidation of the bulk material. While in Area (b) first signs of disorder do already take place, Area (c) displays and disordered state of the material. In area (d) the material suffered severely due to oxidation.

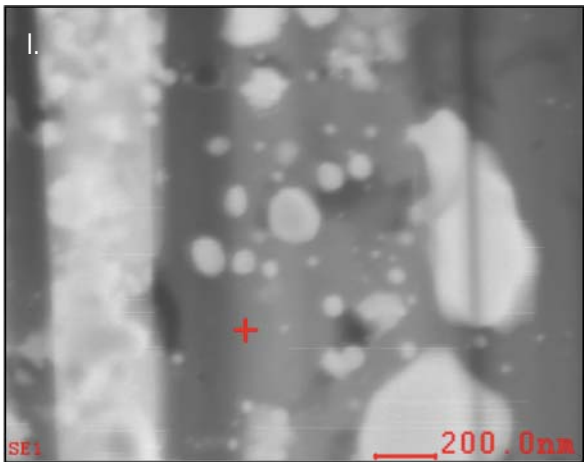

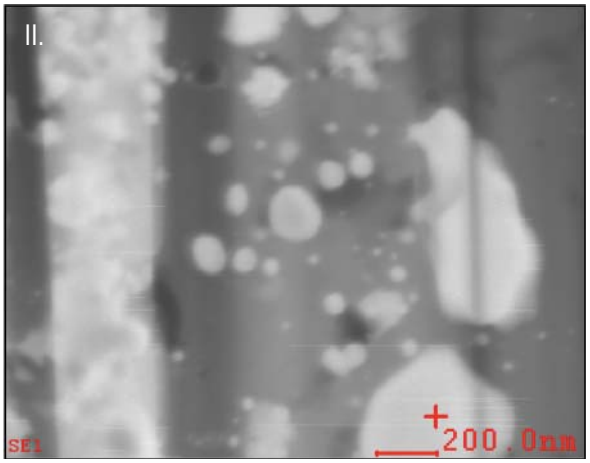

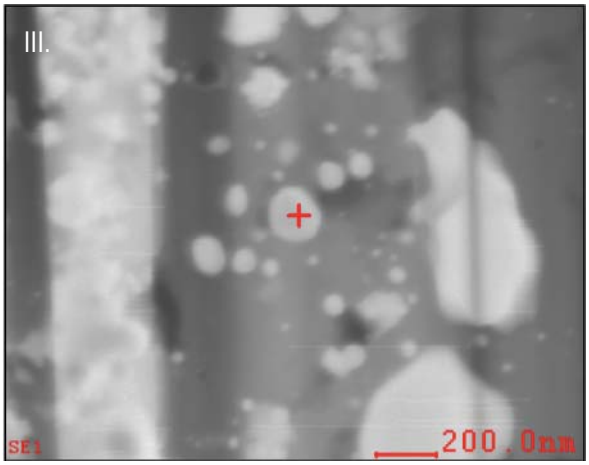

Figure 38 EDX characterization of H1560 (750 °C, 1000 h) of figure 38 area (c). Area 3 displays the most severe changes in microstructure due to oxidation. On the right hand side are the EDX characterizations of the corresponding area. The areas characterized are marked. Picture (I) if figure 38 characterizes the bulk of area (I.III) of figure 37 while picture (II) and (III) characterize various precipitates in the same area.

Table 9: Chemical composition of specific locations in area (c) of figure 37 shown to the left hand side. The table is ordered as followed; first table – area (I), second table – area (II), third table – area (III)

Element	Wt%	At%
O	71,57	81,88
Ni	02,42	00,76
Al	23,99	16,27
Si	01,23	00,81
Cr	00,79	00,28

Element	Wt%	At%
O	51,90	65,33
Al	45,06	33,63
Ni	3,03	1,04

Element	Wt%	At%
O	15,84	32,63
Al	30,45	37,21
Ni	53,71	30,17

The material properties shown below in table 10 were obtained via characterization of the sample using methods and values shown in chapter 1.2 and 2. It was not possible to receive k_0 and Q, which would have given even greater insight into the material, due to the fact that samples exposed to 1000 °C for 24 h did not deliver useful data.

Table 10 Material data obtained important for oxide growth exposed to 750 °C for 1000 h.

Material	Oxide	s [m]	k_p' [m^2/s]
H214	Al_2O_3	$60 * 10^{-6}$	$1 * 10^{-15}$
	Cr_2O_3	$40 * 10^{-6}$	$4.444 * 10^{-16}$
	NiO	$90 * 10^{-6}$	$2.25 * 10^{-15}$
H214Al	Al_2O_3	$60 * 10^{-6}$	$1 * 10^{-15}$
	Cr_2O_3	$30 * 10^{-6}$	$2.5 * 10^{-16}$
	NiO	$100 * 10^{-6}$	$2.778 * 10^{-15}$
H1560	Al_2O_3	$30 * 10^{-6}$	$2.5 * 10^{-16}$
	Cr_2O_3	$20 * 10^{-6}$	$1 * 10^{-16}$
	NiO	$40 * 10^{-6}$	$4.444 * 10^{-15}$

3.2.2 High Temperature Exposure to Carbon

H214

The Carbon diffused along the grains into the material. In this case, the diffusion alongside the grains was so rapid that traces of Carbon were found all over the material. The Carbon further diffused from the grain boundaries into the grain itself. The Carbon diffusion at a temperature of 750 °C had a higher impact on the grains close to the surface, than on those closer to the core of the material, while the carbon diffusion at 1000°C left its impact in the whole material (fig. 39). Due to the diffusion of carbon alongside the grain boundaries, a segregation of chromium to the grain boundaries was observed. In addition to a carbon and chromium rich region, a nickel-depleted area was created. This behavior was verified by an elemental map (fig. 40) and line-scans (fig. 41 and fig. 42).

This type of carburization can be often found in environments of low oxygen pressure and was explained earlier. The type of the diffusion for the different temperatures was quite different. While a type B diffusion occurred at 750 °C, it is not safe to assume a specific type of diffusion for the sample exposed to 1000 °C. It can be seen though that the material suffered extensively of carburization (fig. 39). While it was possible to create an informative elemental map for the sample exposed to 750 °C, the task was pointless for the temperature of 1000 °C.

The elemental maps conjointly with the line scan, unveil the diffusion path of carbon alongside the grains into the material and where it formed $M_{23}C_6$ (in this case $Cr_{23}C_6$, Carburization first class)(fig. 39 - 41).

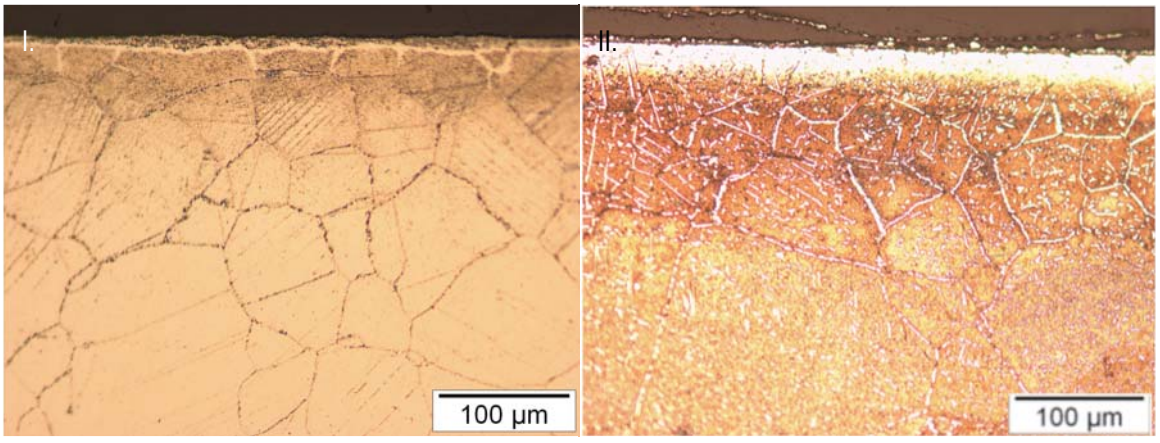

Figure 39 H214 coated with carbon annealed at 750 °C for 1000 h (I) and at 1000 °C for 24 h (II).

The line-scan of H214 annealed at 750 °C, displays a rapid and significant increase in the chromium content at each grain boundary, while the nickel content is decreasing (fig. 42). Some carbon spikes can be observed. Carbon and oxygen are unfortunately hard to detect with the energy dispersive X-ray spectroscopy. Nickel depletion at the grain boundaries and a chromium and carbon increase can be observed, which suggest that $Cr_{23}C_6$ precipitates were formed at the grain boundaries.

The line scan for the sample exposed to 1000 °C, proves that the whole cross section of the sample was effected by the diffusion of carbon (fig. 42). Chromium segregations and nickel depleted areas were observed. The reason why this material suffered so extensively of the diffusion of carbon might be explained by the link of the activation barrier to the temperature [22].

In order to identify the precipitates, an area around a grain-boundary was chosen and characterized using FIB and STEM (fig. 43, fig. 44 and table 11). Note that high concentrations of carbon and silicon are measured, which do not represent the actual concentrations of the elements in the materials but can be explained as background artifacts. Nevertheless the carbon concentration is somewhat higher in the precipitate than in the matrix of the material which leads to the conclusion that the precipitate is a carbide The line - scan for the sample annealed at 1000 °C (fig. 42) contains chromium and nickel concentrations. It does indicate that wherever there is a chromium increase there is a nickel depletion, which could be explained by the forming of chromium carbides. As seen in the previous element map, carbon affects both the grain-boundaries and even the bulk of the material itself. A suitable area at a grain boundary was chosen and prepared in order to conduct the characterization of a precipitate.

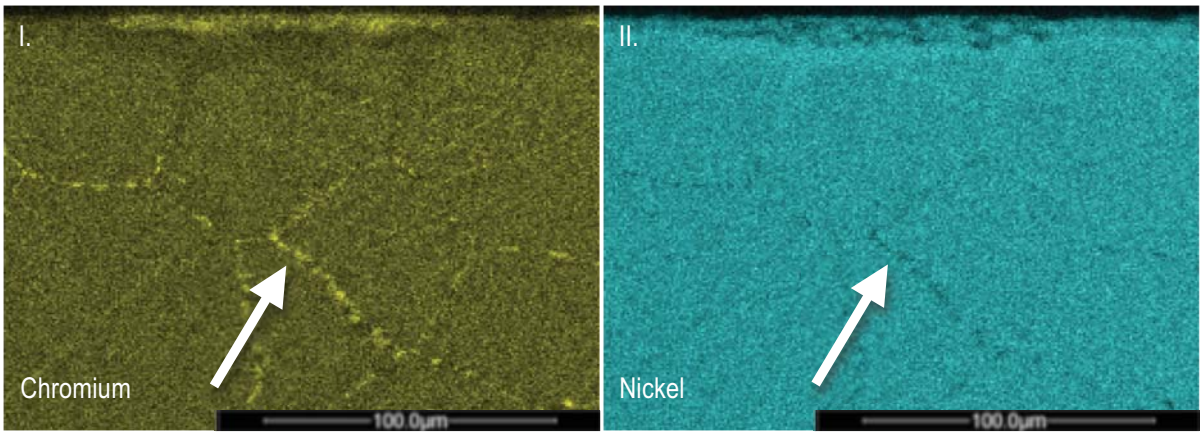

Figure 40 Chromium and nickel distribution in H214 carbon coated, annealed in vacuum at 750 °C for 1000 h. Note the higher density of chromium as well as the nickel depletion at the grain boundaries (arrow).

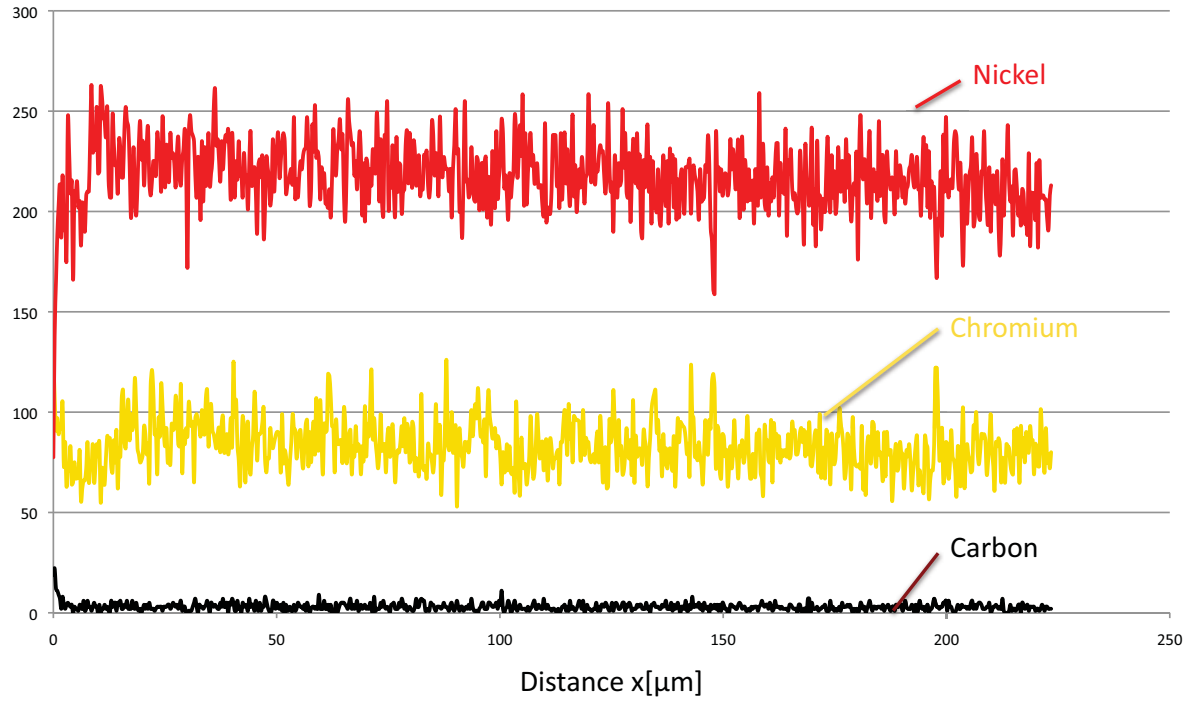

Figure 41 Line-scan of the effected area in H214 carbon coated annealed in vacuum at 1000 °C for 24 h. The chromium - carbides are clearly visible due to the drastic decrease of nickel and the chromium spikes each time a grain - boundary or chromium - carbide is crossed.

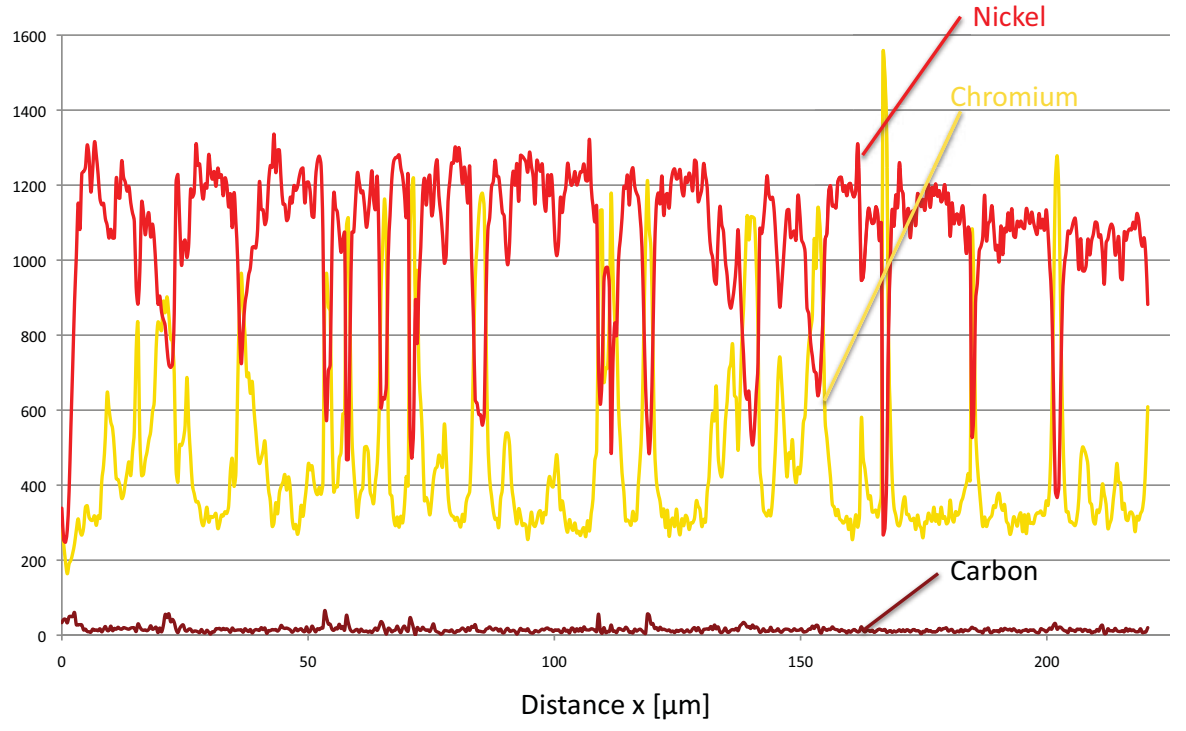

Figure 42 Line-scan of H214 carbon coated annealed in vacuum at 750 °C for 1000 h. Note the chromium segregations at the grain boundaries. Each time, the line-scan crosses a grain boundary, the nickel content is decreasing as carbon and chromium content is increasing.

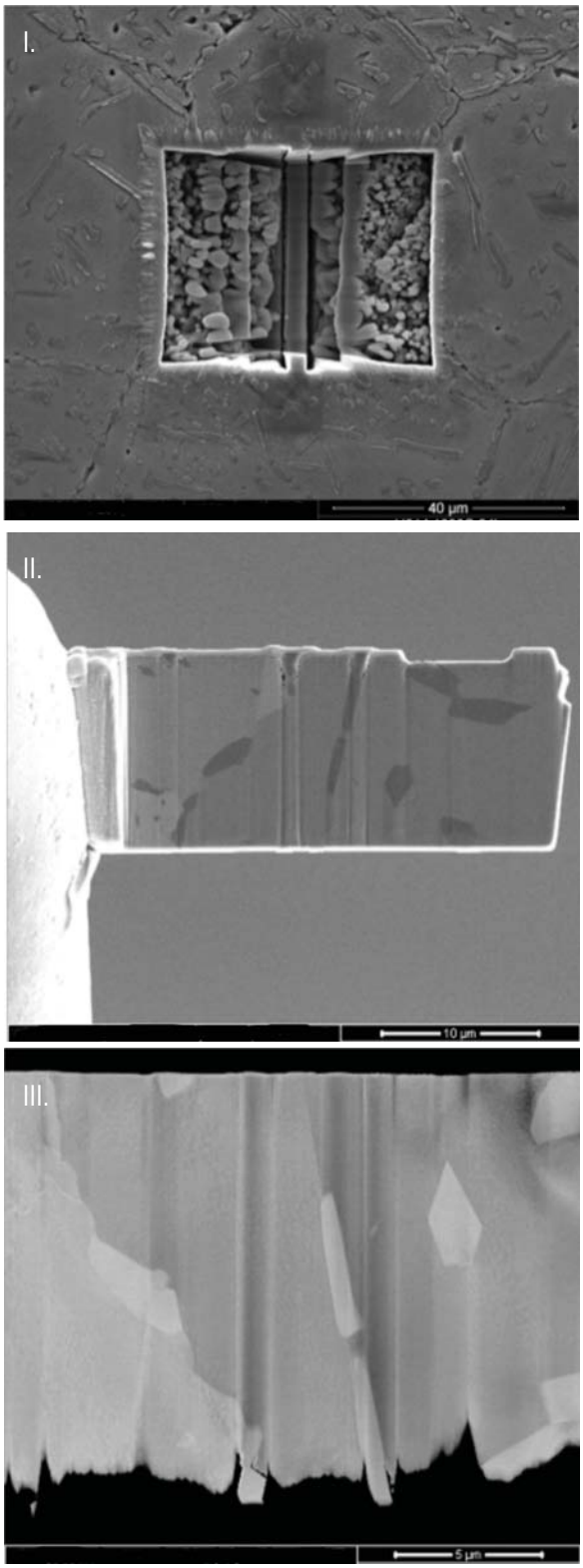

Figure 41 Displayed are various stages of the work necessary in order to characterize $M_{23}C_6$ precipitate using FIB and STEM methods. (I) Area chosen from the sample, in order to conduct a characterization. (II) Sample was welded to sample holder. (III) Start of sample characterization.

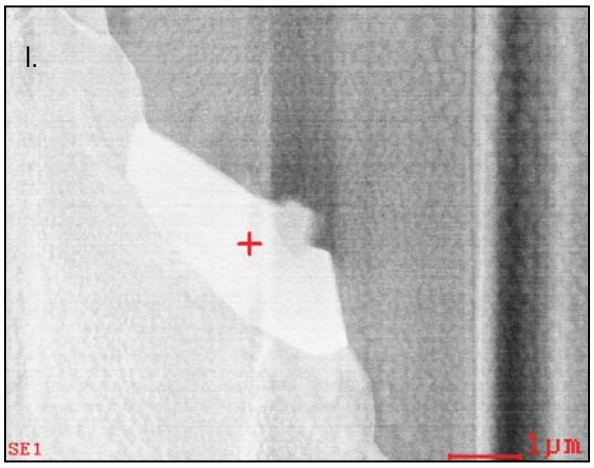

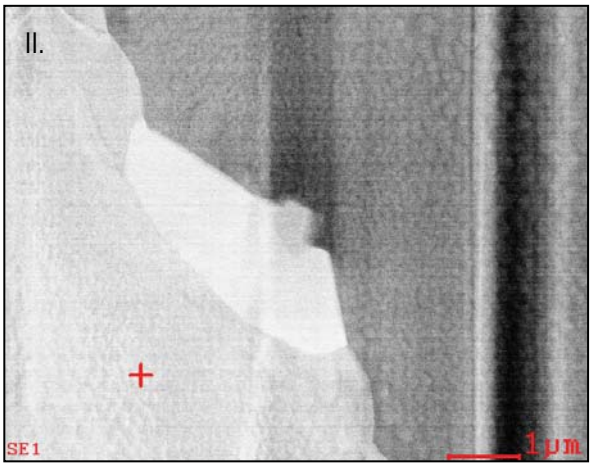

Figure 42 $Cr_{23}C_6$ particle and Matrix of H214C annealed at 1000 °C for 24 h. The pictures display the areas used for the EDX characterization. Particle embedded in H214 (I) and the matrix of H214 itself (II). The EDX characterization is shown on the right hand side corresponding to each figure.

Table 11: Elemental composition as received from EDX point characterization. The data shown in table 1 was retrieved of area (I) figure 44 while table 2 provides data retrieved from area (II) of figure 44.

Element	Wt%	At%
C	53,19	80,88
Al	6,73	4,55
Si	2,05	1,43
Cr	34,96	12,28
Ni	3,07	0,95

Element	Wt%	At%
C	45,49	75,71
Al	11,66	8,64
Si	2,71	1,93
Cr	4,34	1,67
Fe	1,05	0,38
Ni	34,29	11,68

H214Al

It is obvious on first sight, that the diffusion behavior in H214Al is slightly different than in H214 (fig. 45). This change of behavior might be explained by the fact that H214Al was aluminized. The aluminization process did alter the crystal microstructure, which made it harder for carbon to advance into the grains themselves. In accordance with the knowledge that large grains do hinder the diffusion of carbon due to the fact that there are fewer pathways; in this very case, grain boundaries. The obtained simulation results also indicate that carbon is going to avoid aluminum rich areas.

Taking these considerations into account, it is reasonable to assume that the fig. 45 area 1 displays diffusion type B. Carbon is diffusing, using the grain boundaries, but due to the limited numbers of pathways, it is forced to diffuse from the surface into the bulk of the material. Therefore a diffusion front can be observed, starting at the surface into the bulk of the material. The path of diffused carbon atoms can be followed; using either the elemental map (fig. 46 and fig. 47) or the line scans (fig. 48 and fig. 49).

While H214 suffered severe damage due to carburization, the effects on H214Al seam not to be as severe as observed before at a temperature exposure of 1000 °C. Although the carbon diffused through the whole sample alongside the grain boundaries, it didn't affect the bulk of the material as much as it did in H214.

Hence, the diffusion of carbon is mainly alongside the grain boundary and from the surface into the bulk, chromium carbides have been formed at the grain boundaries. Each time the line scan crossed a grain boundary, the chromium content increase significantly, while the nickel content dropped. The crystal itself is not as severely affected as it was in H214.
At the grain boundaries, a TEM foil was cut out, using an ion beam microscope (fig. 50, table 12), to conduct a firm characterization of the material.

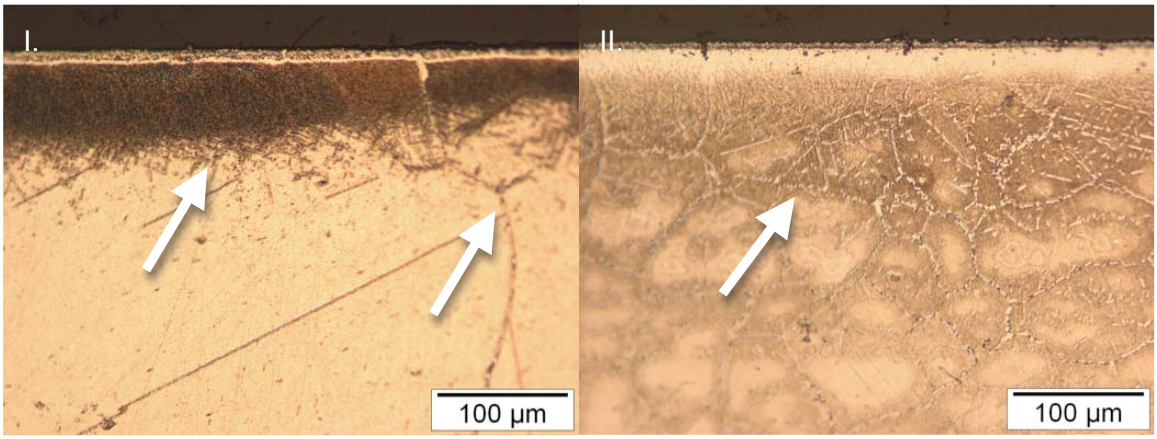

Figure 43 EDX map of H214Al, showing the distribution of chromium and nickel. Areas with local nickel depletion and chromium enrichment are marked. H214Al carbon coated annealed in vacuum at (I) 750 °C for 1000 h and (II) at 1000 °C for 24 h.

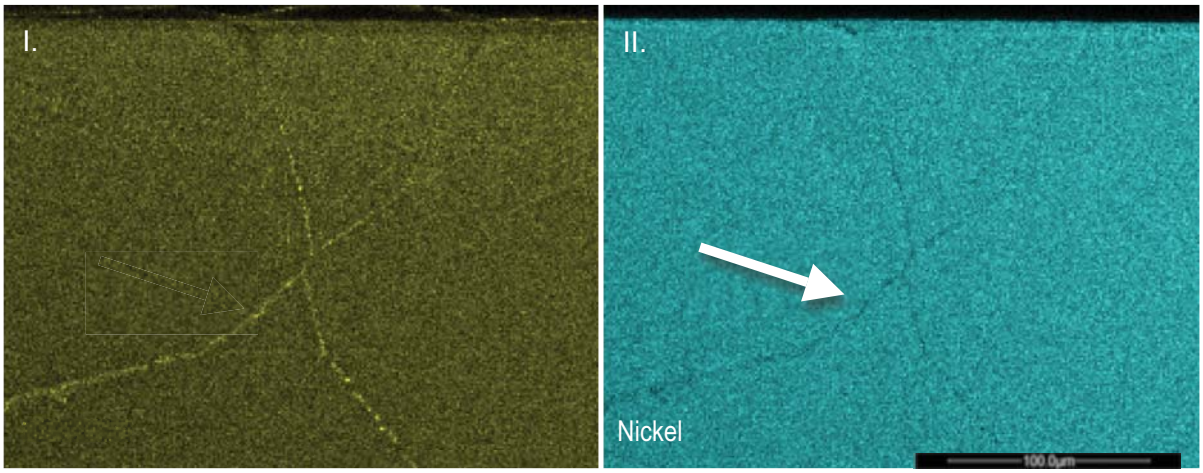

Figure 46 Elemental map of chromium in H214Al carbon coated annealed in vacuum at 750 °C for 1000 hours, showing the distribution of chromium and nickel. Areas with local nickel depletion and chromium enrichment are marked.

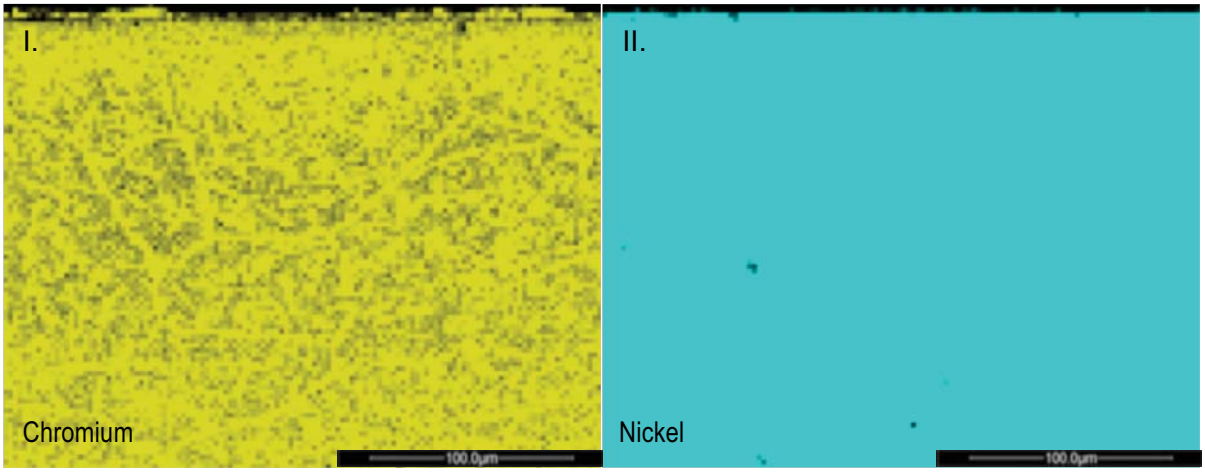

Figure 47 Diffusion front of carbon in H214Al carbon coated annealed in vacuum at 1000 °C for 24 h. The diffusion front of carbon is visible as well as at the grain boundaries.

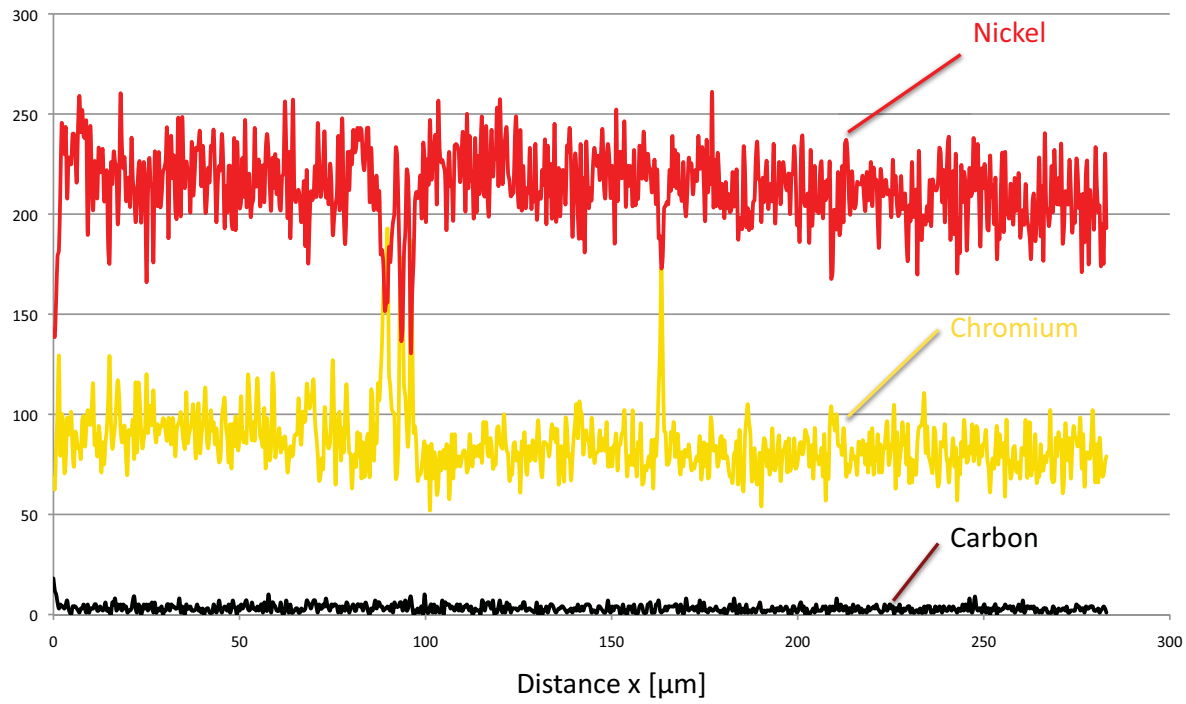

Figure 48 In the line-scan of H214Al carbon coated annealed in vacuum at 750 °C for 1000 h, the nickel depletion as well as the increase of chromium is clearly visible when the path of the line-scan is crossing a grain boundary.

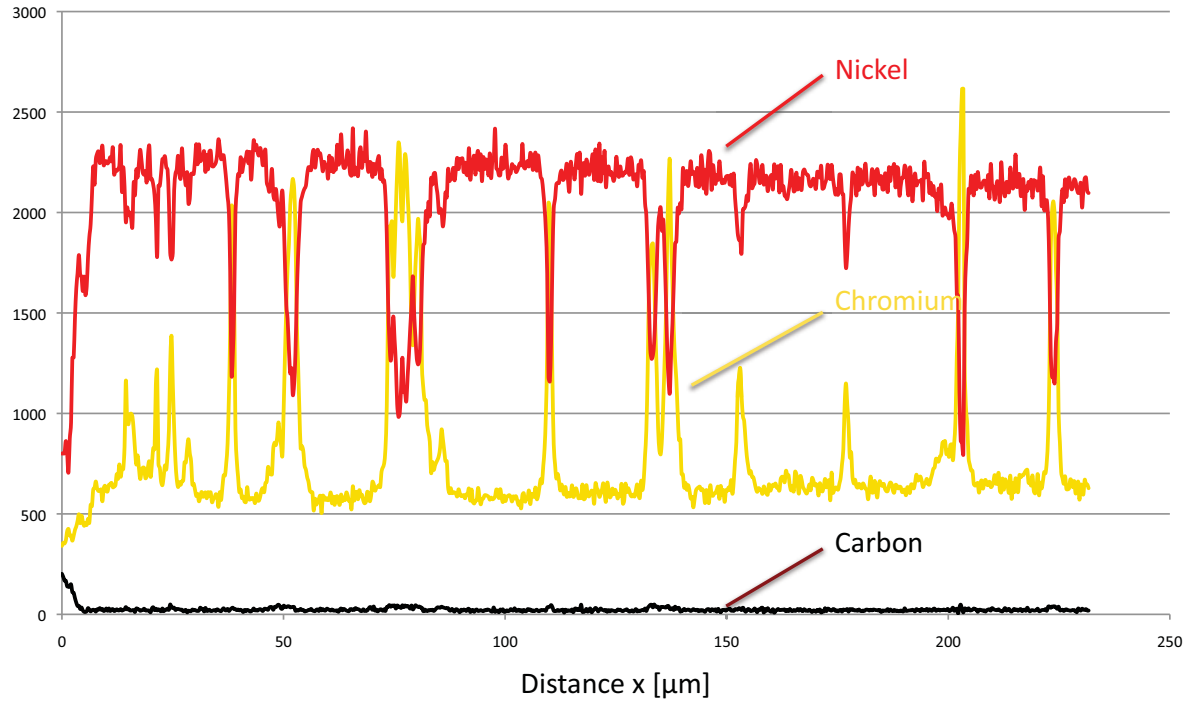

Figure 49 Illustrated is the sample area of H214Al carbon coated annealed in vacuum at 1000 °C for 24 hours used for an elemental characterization performed conducting a line-scan. As seen earlier, each time the line-scan path crosses a chromium-carbide the chromium and nickel peaks pike each versa. This is clearly visible due to the drastic decrease of nickel and the increase of chromium.

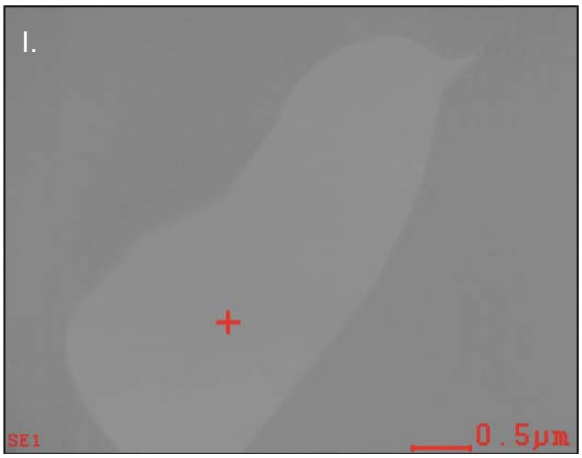

Table 12: Data received by EDX characterization of H214Al - matrix annealed at 1000 °C for 24 h. Table 12.1 displays data obtained in area (I) of figure 50 while table 12.2 contains data of area (II) of figure 50.

Element	Wt%	At%
C	51,46	79,15
Al	8,82	6,05
Si	2,74	1,80
Cr	33,86	12,03
Ni	3,13	0,99

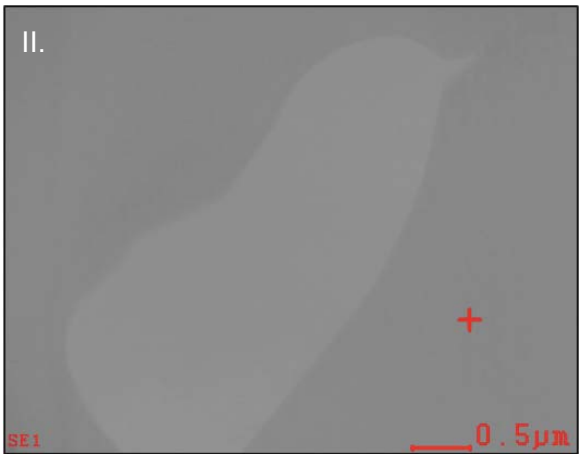

Element	Wt%	At%
Al	26,33	41,43
Si	5,82	8,80
Cr	6,87	5,62
Fe	1,82	1,38
Ni	26,44	17,67

Figure 44 EDX characterization of a particle in H214Al (I) and of the H214Al - matrix (II) annealed at 1000 °C for 24 h

H1560

H1560 is a nickel based single crystal with a high fraction of Ni_3Al. The volume fraction of Ni_3Al is thought to be 70 volume-percent, ensuring an optimal high creep behavior. The nickel-matrix and Ni_3Al precipitates are forming a coherent interface, which only allows similar diffusion properties, common in a bulk system. The microstructure and the composition of the experimental alloy H1560 is as close to the simulation as it could possible be for a technical material. Therefore the behavior of carbon and oxygen is of uppermost importance.

Although the material was exposed to the same conditions, as every other material, there were no obvious visible effect on the material after exposure to 750 °C nor to 1000 °C. The only visible effect was the loss of coherence in some areas (marked in fig. 51) due to the growth of Ni_3Al.

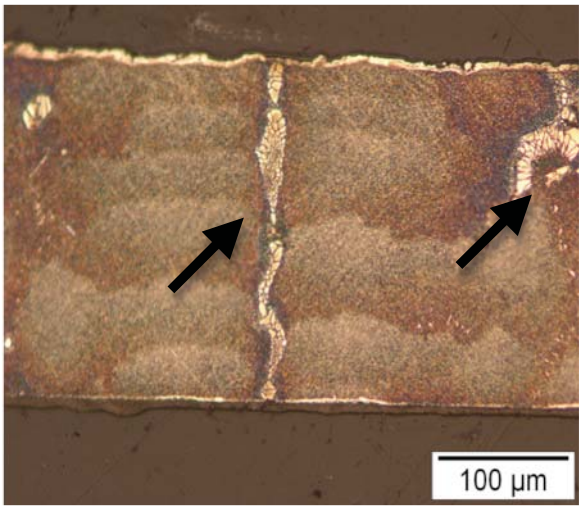

Figure 45 H1560 annealed at 1000 °C for 24 hours. Note the marked areas, which show the crystal growth of Ni_3Al.

Characterizations conducted, using SEM and EDX, did not achieve reasonable results. Hence the focus ion beam in STEM mode was used in order to retrieve appropriate results (fig. 52). It was possible to see carbon particles by using the FIB in a STEM mode.

In the first area of the sample, precipitates were clearly visible. Those precipitates were later identified as carbides (fig. 53, table 13). It appears that carbon is not affecting the Ni_3Al phase, but instead, it is trying to work its way around them. It diffuses alongside the Ni - matrix and the Ni_3Al phase, but not into the Ni_3Al phase.

Diffusing alongside the coherent interfaces hinders carbon from dispensing faster into the bulk, which is the reason why the whole material is not as corrupted by the carbon diffusion as H214 or H214Al. There is no pathway in form of a grain boundary or defects, which carbon could use in form of ”pipe diffusion” and the circumstance of a very high aluminum content might also hinder the advance of carbon in the material. These findings are also in accordance to the simulated results. The simulation results further indicate that the diffusion path of carbon is going to be in the nickel rich phase, avoiding the Ni_3Al phase and therefore will be located at the interface of Ni and Ni_3Al in 100 orientation.

As can be seen in fig. 52, the higher the concentrations of carbon, which Ni_3Al is exposed to, the less ordered Ni_3Al appears. The carbon concentration is affecting the ordered interfaces by starting to disarray and dissolve them. While a perfect order of Ni and Ni_3Al in a 001 - orientation remains in non-affected areas of the material. There is evidence, that carbides are not randomly placed, but instead aligned in the 001 orientation of the cubic lattice. This result was anticipated after processing of the simulated results.

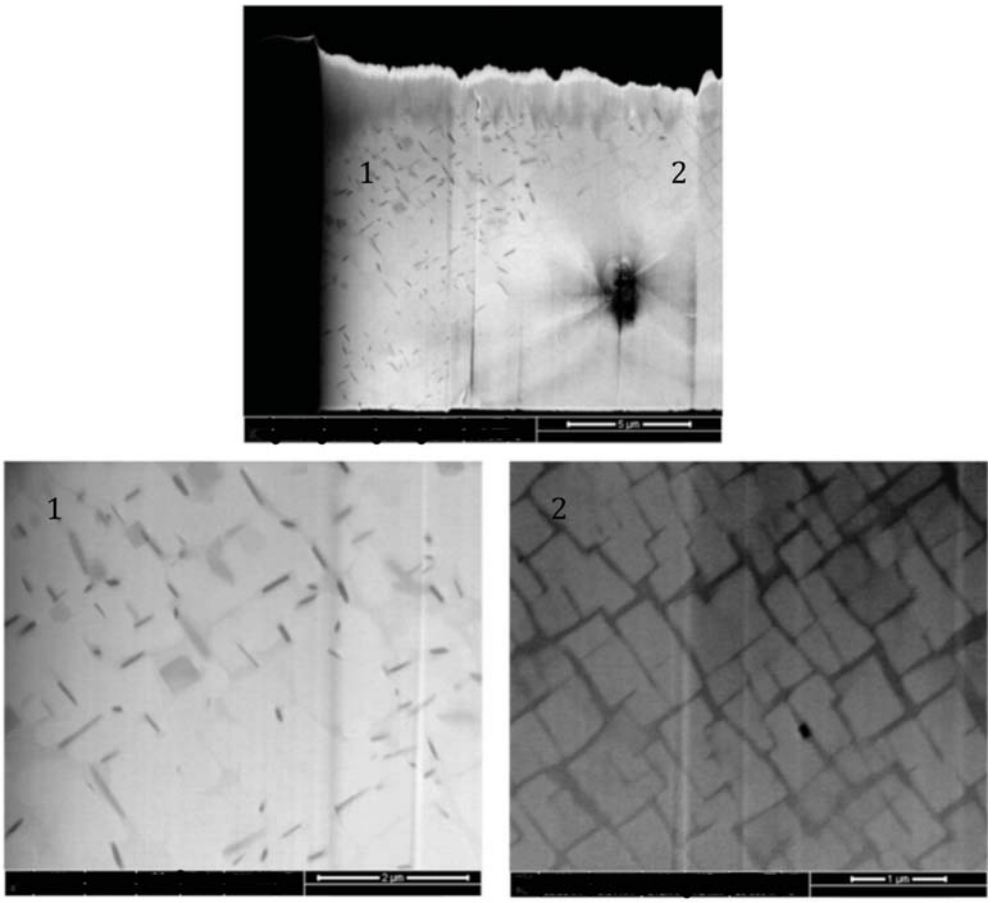

Figure 46 STEM pictures of H1560. Note the carbides ordered in 001 orientation in area (1). Area (2) displays an unaffected Ni – Ni_3Al zone.

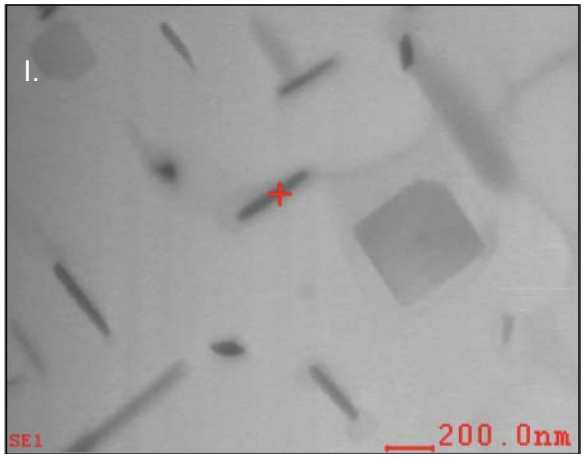

Table 13 Elemental characterization of a carbon-affected area in H1560. Table 13.1 obtains data found in a precipitate of area (I) of figure 53 while table 13.2 displays data of area (II) of figure 53.

Element	Wt%	At%
C	35,98	64,44
Al	6,74	5,39
Si	30,24	23,16
Cr	1,24	0,51
Ni	13,95	5,11
Ta	11,84	1,4

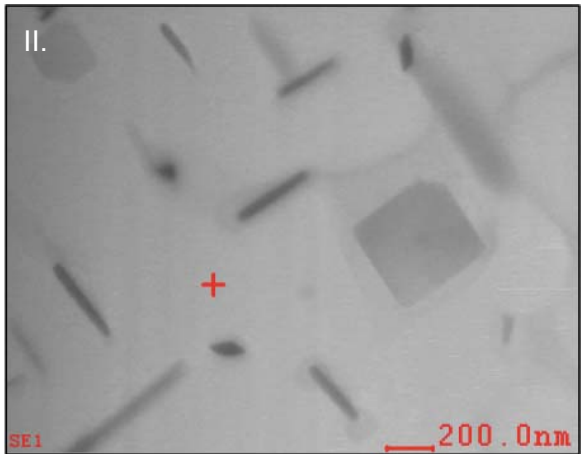

Element	Wt%	At%
C	39,25	65,16
Si	33,67	23,91
Cr	0,77	0,29
Ni	17,46	5,79

Figure 47 EDX characterization of carbon affected areas in H1560 (750 °C 1000 h). The characterized areas are marked by a read cross.

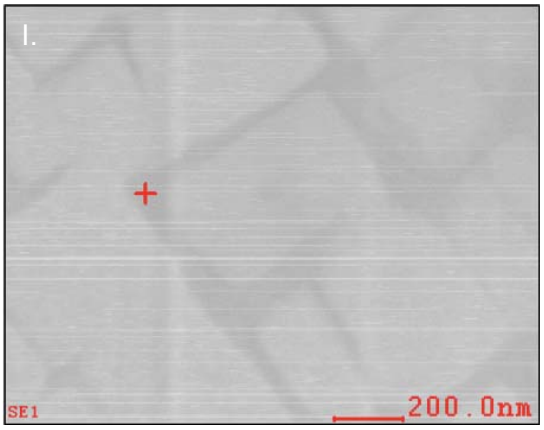

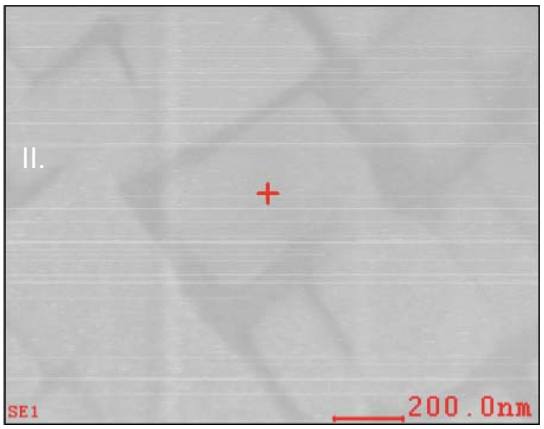

Figure 48 EDX characterization of carbon unaffected areas in H1560 (750 °C 1000 h). Area (I) characterizes a γ - phase while area (II) obtains data of a γ' - phase.

Table 14 Elemental characterization of a carbon-affected area in H1560. Table 14.1 obtains data of area (I) of figure 54 (γ - phase) while table 14.2 displays data of area (II) of figure 54 (γ' – phase).

Element	Wt%	At%
C	45,96	67,61
Al	7,55	4,94
Si	41,80	26,30
Cr	2,40	0,81
Ni	11,08	3,33

Element	Wt%	At%
C	39,94	65,86
Al	7,24	5,31
Si	39,59	27,92
Cr	1,15	0,44
Ni	11,18	0,38
Ta	0,9	0,09

Due to the fact that a tracer diffusion testing was not possible, only a limited amount of data can be salvaged from the high temperature exposure to carbon. The data characterization can be seen above. All data that is possible to be obtained can be seen below in table 15.

The behavior of carbon in H1560 is of importance due to the fact that it conforms the expected behavior suggested by simulation.

Table 15 Behavior of carbon in H1560 annealed at 750 °C for 1000 h

Material		s [m]	k_p' [m^2/s]
H1560	C	$30*10^{-6}$	$2.5*10^{-16}$

4. Discussion

To verify our methods and improve our results, we compared our calculations to those completed already during the research of Y. Mishin et al. [33]. A Ni_3Al 2x2x2 super cell was constructed and a Ni vacancy was created in the system as well as an Al vacancy in a similar system.

The compared results (fig. 54) had a small mismatch. This mismatch of the results can be explained by the use of

(i) different pseudo-potentials
(ii) different k-point grid
(iii) different E-cut

Unfortunately, those values used by Mishin were not accessible and could not be re-evaluated. Therefore, we considered our calculations as accurate and continued our research.

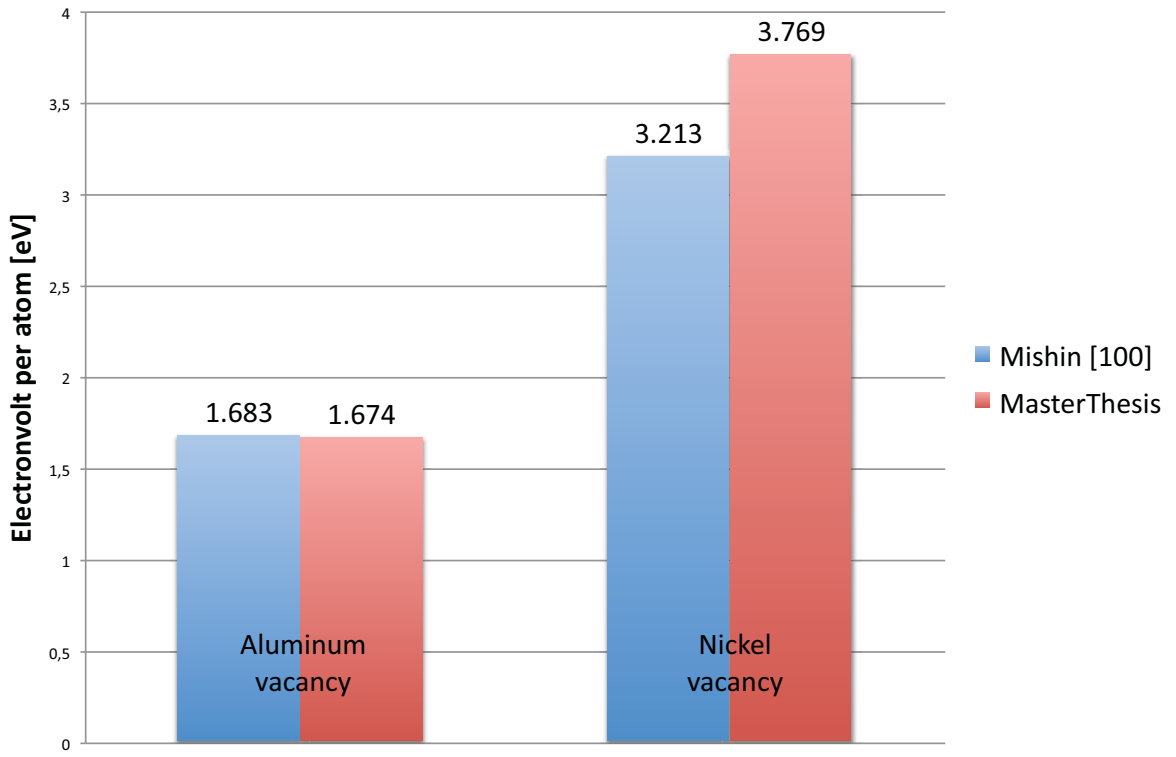

Figure 49 Comparison of the simulation approach with previous studies conducted by Mishin, on the point defect formation energy in a pour Ni_3Al system by creating a Ni and an Al vacancy.

The diffusion pathways were estimated using our calculations for Ni_3Al (fig. 23, fig. 24, fig. 25) and simulation results of figure 56 [34]. The simulated results obtained compare well with each other, although the modified embedded atom model (MEAM) was used instead of VASP.

Unfortunately, it was not possible to conduct further nudged elastic band (NEB) calculations in order to retrieve a better diffusion pathway and more accurate diffusion energy barriers due to restrictions in computational resources. Therefore, the diffusion path (fig. 25) is only an estimation based on the point defect energies.

In retrospective, it would have been a wise choice if the diffusion simulations had been conducted using MEAM due to the fact that different temperatures and larger systems would have been able to be simulated. However to conduct a simulation, it is necessary to have the right pseudo potentials for the prospective simulated system. Regrettably, MEAM is a rather new approach and requires pseudo potentials compatible to its configuration, which have not yet been developed. Hence there was no other choice left than to use VASP.

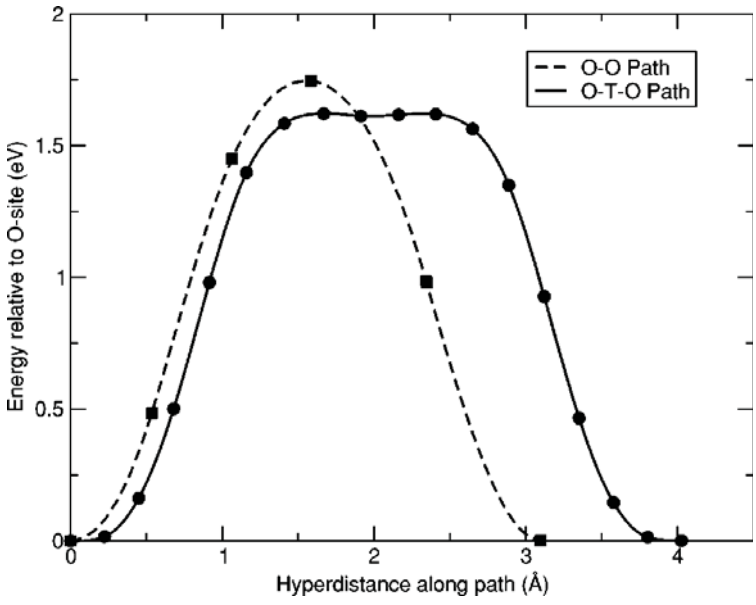

Figure 50 Activation energy for C interstitial diffusion between octahedral sites between two different pathways in a pure nickel system [33].

The simulation predicts that the diffusion path of carbon is going to be inside the nickel rich phase, while it rather chooses not to diffuse into the Ni_3Al phase if possible. It is therefore reasonable to find carbides at Ni - Ni_3Al interfaces, which can bee seen in figure 52.

This result and the confirmation of the behavior of carbon can be also seen in figure 57 [1]. The behavior of carbon in nickel based super alloys was characterized using electro diffraction pattern, where the $M_{23}C_6$ carbides were perfectly aligned with the cubic lattice edges of Ni - Ni_3Al interfaces.

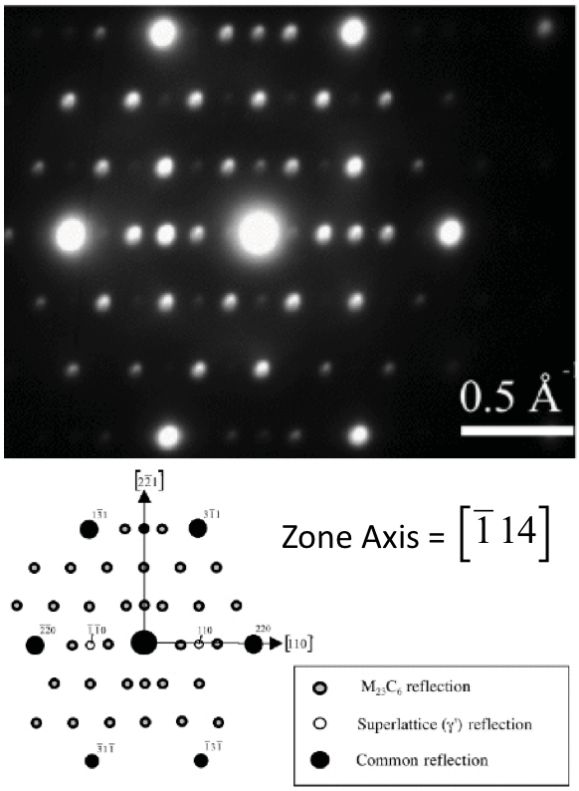

Figure 51 Superimposed electron diffraction pattern from γ, γ ', and $M_{23}C_6$ carbide. The γ and γ ' phases have their cubic-lattice edges perfectly aligned [1].

5. Conclusion

The aim of this thesis was to investigate and understand the behavior of interstitial elements in Nickel super alloys and to create a database necessary for future studies. The work was focused on aluminum rich areas, which are important for the development of Ni_3Al. Ni_3Al is responsible for the high temperature creep resistance. Therefore three materials were selected H214, H214Al and H1560.

To achieve valuable results using VASP simulation program, it was decided to use a 3x3x3 unit cell with 108 atoms. This unit cell would have had further positive aspects if a grain boundary could have been successfully simulated. Adding one atom of each species simulated the interstitial element.

No results could be obtained of the samples treated at 1000 °C for 24 hours at air due to the high incubation time of oxygen. Furthermore, no carbon was found in H1560 treated at 750 °C for 1000 hours exposed to Carbon, due to the high dislike of carbon towards aluminum and the fact that the single crystal offered no diffusion path for carbon. Instead, bulk of the material acted like a single grain.

The carburization tests were conducted in vacuum, which leaves room for improvement by adding an inert gas into the quartz-tube. The inert gas is going to alter the gas pressure, which might lead to a different type of carburization.

The simulation results obtained, suggest a dislike of carbon towards aluminum. Henceforth, carbon is going to avoid aluminum-rich areas, opting instead for a nickel-rich matrix. Oxygen has a high affinity for aluminum atoms in comparison. Those results were helpful in understanding, why certain areas were affected by carburization, while others remained unharmed and were used to assess the deep impact of oxygen. The high growth kinetics of nickel-oxide and affinity of nickel towards oxygen and the ability of nickel to diffuse faster to the surface than it is able to diffuse inside the bulk material, results in a nickel-oxide layer on the surface aside of a nickel depleted area inside the material itself. This behavior leads to the observed Kirkendall effect.

However, the simulation is of limited use due to the small-sized system, which can be simulated. The results may only be accurate for bulk systems and coherent interfaces, while being relatively unimportant in terms of materials with grain boundaries with a large mismatch. Other materials than nickel and aluminum weren't taken into account due to the limitation on the system size. Yet, graphic evidence from the experiments show that chromium plays an important role in the diffusion of carbon by forming $Cr_{23}C_6$ at the grain-boundaries and forming a continuous Cr_2O_3 layer.

In certain ways, the simulation allowed to almost unerringly predict the behavior in the materials before even conducting the experiments. As calculated beforehand during the simulations, carbon does require a high amount of energy in order to be placed in an aluminum rich area. While in H214 carbon not only formed $Cr_{23}C_6$ at the grain boundaries, it also diffused into the grain itself. H214Al on the other hand, with a twice as high aluminum content as H214, was not as severely affected by carbon as H214. $Cr_{23}C_6$ formed alongside the grain boundaries, while carbon had not yet affected the grain itself completely.

H1560, with its well-ordered microstructure, forced carbon to diffuse alongside the coherent Ni-Ni_3Al interfaces into the bulk material. The inability to use large mismatches of the grain boundaries, forced the carbon to diffuse alongside high aluminum rich areas, which slowed down its diffusion process dramatically. Therefore, no carburization effects could be observed with optical microscope, SEM or EDX. Using STEM, it was possible to find traces of carbon alongside Ni_3Al in the nickel bulk, however the Ni_3Al phase itself was not influenced.

The simulation results predicted the behavior of oxygen and carbon in H1560 well, but can only be taken as rough estimations for H214 and H214Al. The simulations do achieve quite good results for binary systems, but due to the restrictions in the system size it was not possible to simulate a three elemental system. The results do prove to be quite accurate for the behavior of carbon for nickel based single crystal with a high volume percentage of Ni_3Al. The obtained results for oxygen are quite interesting, albeit not enough to indicate or predict its behavior in a nickel super based alloy. To achieve this goal more equations have to be taken into account such as the intrinsic defect structure involving cation vacancies and electron holes [20,21,22]. Nevertheless, the obtained simulation data is a very useful starting point to conduct further investigations in this topic. Adding the calculated data to existing data [26-30] for pure nickel could lead to an accurate diffusion profile and diffusion simulation using the Monte Carlo simulation program.

6. Future Prospects

To improve the method for predicting the behavior of interstitial elements in technical materials, several more methods could be implemented. To achieve a better simulation of the technical material, the problematic factors have to be located first.

With the current codes available, it is not advisable to calculate systems with more than two main elements. Therefore several systems have to be created in which several steps of the reaction inside the material can be simulated.

The interaction of interstitial elements towards each other should be taken into account in order to effectively predict their behavior (e.g. forming of carbides).

Transition state theory - the calculation of transitions like the diffusion in solids - must be conducted to allocate possible pathways. Especially, the formation and migration energy for interfaces would need to be calculated to gain information on the behaviour of interstitial elements at grain boundaries and interfaces in order to observe if elements are going to diffuse into the next grain or interface or if they are going to enrich along the grain boundary (fig. 57).

It would be also interesting to know the embrittlement of a grain boundary due to diffusion. Therefore the formation energy of several grain boundaries has to be calculated and compared. For a first step, the energy of a grain-boundary without any interstitial atoms is calculated. In the second step, an interstitial atom is implanted in the near the grain boundary. The formation energies are going to be compared and analysed.

During the next step, a gap of at least 10 Å (so that there is no interaction between the systems), is produced between the grain and the procedure is repeated. Because of the gap, it is possible to calculate the cleavage energy and how the interstitial atom affects it. The cleavage energy provides information about brittleness of the material. Using those combined methods it should be possible to approximate the simulation of a technical material.

A newly developed approach, which is not as generally known at the kinetic Monte Carlo (KMC), is the *modified embedded-atom* method or MEAM. Unfortunately, it hasn't been commonly exploited, hence only a few pseudo-potentials are available for usage.

Simulations could be further used not only for the prediction of the possibility of corrosion in certain environments, but furthermore to calculate the expected thickness or the growth-rate of a self-protecting layer or the live-expectancy of the materials. The generalized-gradient approximation (GGA) [34, 35] could be used to estimate tensions in an oxide layer, which enables to predict a possible failure and the mechanical properties of an oxide layer and therefore would predict corrosive resistance in dependence to temperature.

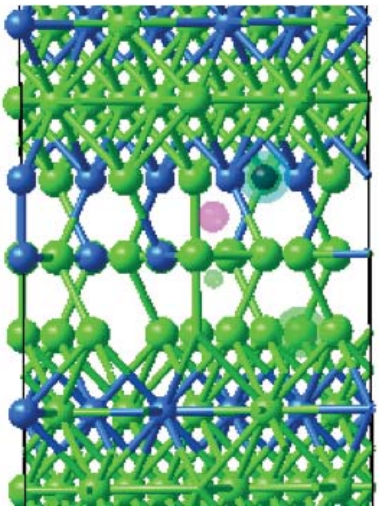

Figure 52 Tilted Grainboundary of a Ni_3Al system with an interstitial C atom and two spheres of possible positions α=7,98°

7. Literature

[1] H. Bhadeshia, Nickel Based Superalloys, www.msm.cam.ac.uk/ phase-trans/2003/Superalloys/superalloys.html (Online accessed March 15 2009)

[2] H. Cloodt, Signs of recovery for air transport in Europ in 2009, eurostat Statistic in focus, 02/2011

[3] M.Chapman, Jet Propulsion, www.bloodhoundssc.com/car/jet_propulsion.cfm (Online acessed Feb. 2011)

[4] P. Saltikov, Hochtemperatur-Termochemie im System Al-Cr-Ni-O, Max-Planck-Institut für Metallforschung, 05/2003

[5] Military.com – All the benefits of the service, http://shock.military.com/Shock/gallery/images.do;jsessionid=BFDE0068E72799105C40BD2DECB58DBF (Online accessed March 2010)

[6] Life Prediction Technologies, Inc., www.lifepredictiontech.com/images/turbine_blade.jpg (Online accessed March 2010)
MATCO Services, Inc., Electric Power Industry – Asset Management, www.matcoinc.com/failure-analysis/electric-power, (Online accessed March 2010)

[7] M. Durand-Charre, “The microstructure of superalloys”, Gordon and Breach Science Publishers, 1997, p. 17, 105

[8] MedeA User Guide, Materials Design Inc., 2008, p. 172 – 182

[9] R.B. Phillips, Crystals, Defects and Microstructures – Modeling Across Scales, Cambridge University Press, pp. 149 - 206

[10] J.F. Janak, Proof that $\partial E / \partial n_i =$ in density – function theory, Phys. Rev. 18 (1978), p. 566

[11] F.K. Schulte, On the theory of the work function, Z. Phys. B27 (1977), p. 303

[12] U. von Barth, L. Hedin, A local exchange-correlation potential for the spin polarized case, J. Phys. C. 5 (1972), p. 1629

[13] D.D. Koelling, B.N. Harmon, A technique for relativistic spin-polarised calculations, J. Phys. C. 10 (1977), p. 3107

[14] http://en.wikipedia.org/wiki/Brillouin_zone (Online accessed August 15 2010)

[15] www.iue.tuwien.ac.at/phd/hackel/_3462_figure895.gif, (Online accessed August 15 2010)

[16] http://en.wikipedia.org/wiki/Pseudopotential (Online accessed August 15 2010)

[17] O.I. Gunnarsson, B. Lundquist, S. Lundqvist, Exchange and correlation in inhomogeneous electron systems, Solid State Communications 11 (1972), p. 149

[18] A.D. Becke, Density-functional exchange-energy appromixmation with correct asymptotic behaviour. Phys. Rev. A. 38 (1988), p. 3098 - 3100

[19] H. J. Grabke, “Hochtemperaturkorrosion von Metallen durch Reaktion mit Gasen”, “Korrosion und Korrosionsschutz” (ed. E. Kunze), Wiley-VCH, Band 1 pp. 573 - 648

[20] H. Hindam, D.P. Whittle, Microstructure, Adhesion and Growth Kinetics of Protective Scales on Metals and Alloys, Oxidation of Metals, Vol.18, 1982, pp. 245 - 284

[21] R. Bürgel, “Handbuch Hochtemperatur Werstofftechnik”, Vieweg+Teubner, pp. 24, 270, 271, 296

[22] N. Birks, G.H. Meier, F.S. Pettit, High Temperature Oxidation of Metals, Cambridge University Press, pp. 112, 116, 272,332

[23] R.C. Reed, “Superalloys, Fundamentals and Application”, Cambridge University Press, pp. 309

[24] J. L. Smialek, G. H. Meier, “High-Temperature Oxidation”, Superalloys II – High-Temperature Materials For Aerospace And Industrial Power (ed. C.T. Sims, N.S. Stoloff, W.C. Hagel), A Wiley-Interscience publication, John Wiley & Sons, Inc.

[25] U. Heubner, “Carburisation”, Nickel Alloys, Marcel Dekker Inc (2000), p. 149

[26] L.G. Harrison, Trans. Faraday Soc. 57 (1961), 1191

[27] Y. Mishin, C. Herzig, Grain boundary diffusion: recent progress and future research, Materials Science and Engineering A260 (1999), 55-71

[28] Defects and Diffusion in Metals, Vol. 3 (1969)

[29] Defects and Diffusion in Metals, Vol. 4 (1970)

[30] D.J. Siegel, J.C. Hamilton, First-principles study of the solubility, diffusion and clustering of C in Ni, Physical Review B 68 (2003)

[31] Y. Mishin, A.Y. Lozovoi, A. Alavi, Evaluation of diffusion mechanisms in NiAl embedded-atom and first principle calculations, Physical Review B 67 (2003)

[32] http://en.wikipedia.org/wiki/Birch%E2%80%93Murnaghan_equation_of_state (Online accessed Feb.19, 2011)

[33] Y. Mishin, Atomistic modeling of the γ and γ′-phases of the Ni–Al system, Acta Mater. 52 (2004), 1451-1467

[34] J.F. NYE, Physical Properties of crystals, Oxford University Press (1960)

[35] J.P. Perdew, J.A. Chevary, S.H. Vosko, K.A. Jackson, M.R. Pederson, D.J. Singh, C. Fiolhais, Atoms, molecules, solids, and surfaces: Applications of the generalized gradient approximation for exchange and correlation, Phys. Rev. B 46 (1992), 6671

[36] J.D. Kuenzly, D.P. Douglass, J.D. Kuenzly and D.L. Douglas, "The Oxidation Mechanism of Ni_3Al Containing Yttrium, Oxidation of Metals 8 (1974), p. 139 - 178

[37] http://cms.mpi.univie.ac.at/vasp/vasp/vasp.html (Online accessed August 15 2010)

[38] M. Kalay, H.H. Kart, S.A. Kart, Elastic properties and pressure induced transitions of ZnO polymorphs from first-principle calculations., Journal of Alloys and Compounds, Vol. 484 (2009) p. 431 - 438

[39] M. Nanko, N. D. Thuy, K. Matsumaru, K. Ishizaki, High temperature oxidation of Al_2O_3-based composites with Ni particle dispersion., Journal of Ceramic Processing Research. 3 (2002), p. 132-135

[40] C.L. Fu, G.S. Painter, Point defects and the binding energies of boron near defect sites in Ni_3Al: A first-principles investigation, Acta Mater 45 (1997), p. 481 – 488

[41] G. Kresse and J. Furthmuller, Efficient iterative schemes for ab initio total-energy calculations using a plane-wave basis set Computational Materials Science 6 (1996), p. 15

[42] G. Kresse and J. Hafner, Ab initio molecular dynamics for liquid metals, Phys. Rev. B 49 (1993), 558-561

[43] Y. Amouyal, M. Zugang, D.N. Seidman, Segregation of tungsten at γ' ($L1_2$) / γ(fcc) interfaces in a Ni-based superalloy: An atom-probe tomographic and first-principles study, Applied Physics Letter 93 (2008), p. 201905

[44] E. Cadel, C. Pareige. B. Deconihout, P. Caro, D. Blavette, Phase Transformation and Segregation to Lattice Defects in Ni-Base Superalloys, Microscopy and Microanalysis 13 (2007), p. 464-483

[45] H.H. Kart, M. Uludogan, T. Cagin, DFT studies of sulfur induced stress corrosion cracking in nickel, Computational Materials Science 44 (2009), p. 1236-1242

[46] K.Y. Cheng, D.H. Kim, Y.S. Yoo, C.Y. Jo, T. Jin, Z.Q. Hu, Microstructural Stability of a Single Crystal Superalloy DD8 during Thermal Exposure. J. Materials Science Technology 24 (2008), p. 1-4

[47] P. Lazar, R. Podloucky, Ductility and magnetism: An ab-initio study of NiAl-Fe and NiAl-Mn alloys, Intermetallics 17 (2009), p. 675-679

[48] Y. Saito, H. Harada, The Monte Carlo simulation of ordering kinetics in Ni-base superalloys, Materials Science and Engineering A 223 (1997), p. 1-9

[49] M. F.-X. Wagner, W. Windl. Lattice stability, elastic constants and macroscopic moduli of NiTi martensites from first principles, Acta Mater. 56 (2008), p. 6232-6245

[50] C. Wang, C. Wang, Influence of the alloying element Re on the ideal tensile and shear strength of γ′-Ni3Al, Scripta Materialia 61 (2009), p. 197-200

[51] D. Yang, P. Hodgson, C. Wen, The kinetics of two-stage formation of $TiAl_3$ in multilayered Ti/Al foils prepared by accumulative roll bonding, Intermetallics 17 (2009), p. 727 - 732

[52] C. Wang, C-Y. Wang., Ni/Ni_3Al interface: A density functional theory study . Applied Surface Science 255 (2009), p. 3669-3675